Bifurcations and chaos transition of the flow over an airfoil at low Reynolds number varying the angle of attack

D. Durante[a], E. Rossi[c], A. Colagrossi[a,b,*]

[a]*CNR-INM INstitue of Marine engineering, Rome, Italy*
[b]*Ecole Centrale Nantes, LHEEA research dept. (ECN and CNRS), Nantes, France*
[c]*Basque center for applied mathematics, Bilbao, Spain*

Abstract

The study of an airfoil at low Reynolds number regime was found to be a typical problem where the inception of bifurcations leads the flow evolution from a stationary or periodic behaviour to a purely chaotic one. The present work extends the present literature where numerical investigations of the flow field past two-dimensional symmetric airfoils were performed by fixing the incidence and changing the Reynolds number (Re). Conversely, here the Reynolds number was fixed at Re = 1000 and the angle of attack (AoA) varied from 0° to 90°. Different flow Modes and bifurcation phenomena are detected and, in addition, new non-linear phenomena are also identified. The latter consists of tripling period regimes and its bifurcations up to chaotic conditions. Moreover, for increasing AoA, an inverse transition from chaotic to periodic regimes is also observed. An in-depth study of these different flows is provided and new links with the time evolution of the forces acting on the airfoil, as well as with the wake structures observed, are offered. Phase portrait diagrams are evaluated through the time records of the lift force in order to highlight the eventual presence of limit cycles in the solutions. Accurate numerical simulations are performed with a Vortex Particle Method in a two-dimensional framework, using high spatial resolutions to solve in detail both the near-field and the far-field regions.

Keywords: Flow past stalled airfoil, route to chaos, period doubling and tripling bifurcations, vortex wake, Vortex Particle Method

*Corresponding author: *Tel.:+39 06 50 299 343*
Email address: andrea.colagrossi@cnr.it (A. Colagrossi)

1. Introduction

In recent years, the study of planar flow patterns past various objects has gained a renewed interest. Indeed, the improvements of the flowing soap film apparatuses combined with the use of high-speed camera and low-pressure sodium lamp, allowed the visualization of complex interference patterns (see for example Fayed et al. (2011)). These kind of experimental devices are also widely used for the visualization of the planar flow of the vortical wake of flapping foils Schnipper et al. (2009) or of flexible filament subject to a forced vibration Jia et al. (2015).

Beside the experimental investigations, many numerical studies on planar flow past fixed, moving or deformable bodies can be found in the modern literature (see *e.g.*Wang et al. (2018); Mandujano and Málaga (2018); Bose and Sarkar (2018); Badrinath et al. (2017); Bao et al. (2017); Ye et al. (2017); Das et al. (2016); Krishnan et al. (2016)). Recently, several studies of the flow past airfoils at low and ultra-low Reynolds numbers were published along this investigation strand. In Alam et al. (2010), for example, the near wake characteristics of the flow field past a NACA0012 with varying incidence ($0° - 90°$) are examined and discussed in detail, focusing on vortex formation, wake width, etc. . ..

For low angles of attack (*i.e.* before the stall inception) the 2D assumption is valid also at high Reynolds numbers, as remarked in Lee et al. (2017); Counsil and Goni Boulama (2013); Uranga et al. (2011), where 2D and 3D solutions are compared at Reynolds numbers up to 10^5 and angles of attack lower than $10°$. For higher incidences, the onset of the separation makes the flow field three-dimensional with evident spanwise instabilities even for low Reynolds numbers. Nevertheless, 2D framework studies are worthy of investigation also because of their applicability on low Froude number flows, *i.e.* flow past bridge pylons, flow past little islands, atmospheric stratified flows (see *e.g.* Boffetta and Ecke (2012)). In such a condition the vorticity dynamics at the interfaces is dominated by 2D effects.

Historically, Pulliam and Vastano (1993) were among the first pioneers to study the transition to a chaotic state of the flow field past an airfoil through the increasing of the Reynolds number. In that work the flow past a NACA0012 profile with an incidence of $20°$ was considered in a two-dimensional framework and the Reynolds number within the range 800–1600 was investigated. In particular, the authors identified a *"period-doubling bifurcation to chaos with windows of periodic behaviour in the chaotic regime past Re=1600"*, observed

through the Fourier analysis of the time history of the vertical velocity component recorded in the proximity of the trailing edge (on the suction side).

Recently Deng et al. (2019) discussed the planar flow past a NACA0015 in a low Reynolds number regime (*i.e.* $100 - 1300$) and different angles of attack, spannig from $10°$ to $20°$. When the angle of attack is changed, the system undergoes to an hysteresis, leading to the appearance of different branches on the Strouhal-Reynolds number relationship curves.

Following Pulliam and Vastano (1993), in Rossi et al. (2018) the planar flow past a NACA0010 airfoil at $\alpha = 30°$ was investigated. The Reynolds number was increased from 100 to 3000 and four bifurcations of the solution were identified. Beside the study of the flow field, an analysis of the lift time history was performed in terms of phase portrait diagrams C_l-$\dot{C}_l$ and Fourier transforms.

An interesting investigation of a stalled NACA0012 profile, from the viewpoint of the bifurcations, is performed in Liu et al. (2012). The complex flow around stationary and sinusoidal pitching NACA0012 airfoil at Reynolds 1000 is studied numerically.

Conversely, in Kurtulus (2015) the Reynolds number was set to 1000 and different angles of attack α, ranging from $0°$ to $90°$ were numerically studied. Indeed, the variation of the angle of attack of the profile gives place to peculiar wake topologies and different time behaviors of the forces on the body that will be referred to as Modes. In particular, five distinct flow Modes were observed. Some of those Modes are also detected by Rossi et al. (2018) and connected to bifurcations of the Navier-Stokes solutions.

By increasing α of $1°$ from $0°$ to $41°$, Kurtulus (2015) realized that around $27°$ the lift coefficient time behavior exhibits a dense spectrum of frequencies, thus revealing a transition to chaos. For angles greater than $29°$, a more organized shedding pattern was recovered. Formerly, an analogous chaotic nature of the flow field at $27°$ was found by Khalid and Akhtar (2012). Furthermore, sudden increases in drag and lift coefficients were also observed at $31°$. The vortex pattern for an angle of attack between $30°$ and $31°$ exhibited an abrupt transformation connected to a sudden change in the pressure distribution. The effect of the thickness on the chaotic transition of the wake field was investigated in a recent paper of Kurtulus (2016), where a NACA0002 profile was compared with the former NACA0012. In that study, the ranges of incidence angle related to the different Modes are identified for both airfoils. Moreover, the influence of lateral and longitudinal vortex spacing on the wake stability is also widely investigated and commented.

In the present work, the approach of Kurtulus (2015, 2016) is proposed again,

studying the flow past a NACA0010 airfoil. The Reynolds number is fixed at Re = 1000 whereas the angle of attack is varied from 0° to 90°. In order to get a more depth insight on the bifurcation phenomena the AoA variation is refined within the most interesting ranges. Thanks to this refinement new flow Modes are identified, thus extending the analysis of Kurtulus (2015, 2016). Indeed, beside the period-doubling mode and the transition to chaos (formerly identified by Pulliam and Vastano (1993)), in our analysis a series of tripling period regimes are also found as well as an inverse transition from chaotic to non-chaotic conditions, which is well evidenced.

Similarly to Rossi et al. (2018), in the present study the flow past a NACA0010 airfoil is numerically investigated using a Particle Vortex Method called Diffused Vortex Hydrodynamics (DVH from now on). The latter has been recently developed and extensively validated on numerous benchmark tests, for which the interested reader is referred to Rossi et al. (2015a,b, 2016), Colagrossi et al. (2016) and Durante et al. (2016). This approach allowed the Authors to accurately evaluate both the near and the far flow fields. Indeed, in the numerical simulations considered, high spatial resolutions are used for the near field around the airfoil as well as for the wake region. Furthermore, very long-time computations were carried out in order to achieve an accurate frequency analysis on the time histories of lift force component.

The paper is organized as follows:

- ◇ in section 2 the DVH numerical scheme is briefly recalled;
- ◇ in section 3 the different flow Modes are discussed in terms of wakes topologies, time histories of drag and lift forces, Fourier analysis and Phase portrait diagrams of the lift forces;
- ◇ in section 4 a stability analysis of the Modes is performed, discussing the doubling period, tripling period and the route to chaos behaviour;
- ◇ in section 5 the mean drag and lift are presented as a function of the angle of attack;
- ◇ in section 6 a discussion about three-dimensional effects is depicted;
- ◇ Finally in section 7 conclusions and a plan of future works are sketched.

2. Summary of the numerical method

In this section the Diffused Vortex Hydrodynamics (DVH) method is briefly described. The governing equations adopted in this vortex method are the Navier-Stokes equations written in vorticity ω (Helmholtz equation) which, for a two-dimensional viscous incompressible flow in the domain Ω, read as:

$$\rho \frac{D}{Dt}\omega = \mu \Delta \omega \qquad \forall \boldsymbol{r} \in \Omega, \tag{1}$$

where D/Dt is the material time derivative, whereas ρ and μ are the density and the dynamic viscosity of the considered fluid. In order to solve equation (1), an operator splitting scheme (Chorin (1973, 1978)) is used for taking into account the vorticity field advection and diffusion. These latter are separately considered at each time step. The numerical solution is then obtained by solving an inviscid advective step, governed by the Euler equation:

$$\frac{D}{Dt}\omega(\boldsymbol{r}, t) = 0 \tag{2}$$

followed by a purely diffusive one governed by the heat equation

$$\rho \frac{\partial}{\partial t}\omega(\boldsymbol{r}, t) = \mu \Delta \omega(\boldsymbol{r}, t). \tag{3}$$

The presence of a body within the flow field requires an appropriate procedure. Between the advection and the diffusion steps the vorticity is generated on the body contour in order to enforce the no-slip boundary condition.

The vorticity formulation has several advantages:

i it requires one to discretize only the rotational region of the flow;

ii the boundary conditions at infinity are automatically satisfied;

iii the vortex particles are moved in a Lagrangian way.

During the advective step, the velocity field is decomposed by $\boldsymbol{u} = \boldsymbol{u}_\infty + \boldsymbol{u}_\omega + \boldsymbol{u}'$, where $\boldsymbol{u}_\infty$ is the free stream velocity, $\boldsymbol{u}_\omega$ is the velocity induced by the vortex particles, while $\boldsymbol{u}'$ is the contribution to the velocity field due to the presence of the body. The velocity $\boldsymbol{u}$ is evaluated using a Fast Multiple Method (FMM) (see *e.g.* Cruz and Barba (2009)) and the vortices are displaced using a fourth order Runge-Kutta algorithm. From $\boldsymbol{u}'$ it is also possible to generate a new set of

vortices on the body surface, enforcing the no-slip boundary condition exactly on its contour.

The diffusive step is performed following the deterministic algorithm described in Benson et al. (1989): each vortex particle gives a vorticity contribution on a "Regular Point Distribution" (RPD) by a superposition of elementary solutions of the heat equation. This special set of points will then become the new set of vortex particles substituting the former one.

Because RPDs are sets of points regularly spaced without any topological connection, hence, the DVH scheme can be included among the pure meshless methods. The use of RPDs during diffusion process also prevents the excessive clustering or rarefaction of the vortex particles and avoids remeshing procedures which would be required otherwise (see *e.g.* Barba et al. (2003)). The RPDs around the body are generated using a packing algorithm described in Colagrossi et al. (2012), allowing to arrange points around complex contours while preserving the volume around each point. For further details on the DVH method, please refer to Rossi et al. (2015a,b, 2016); Colagrossi et al. (2016); Durante et al. (2016).

Using the DVH model, the wake is resolved accurately both in space and in time in order to catch the flow Mode dynamics. Despite the fine spatial resolution, the computational costs remain quite limited thanks to the description in terms of vorticity (*i.e.* only the rotational part of the flow field is solved) and thanks to the use of an Adapt Particle Resolution (APR) Rossi et al. (2015a) technique which allows to gradually reduce the particle size in the near-field close to the airfoil. Besides the time/spatial resolution, the simulations should be carried out for a long time in order to reach stable conditions, being some Modes characterized by very long transients (see next sections).

In Appendix A a convergence test of the method is discussed in order to asses the actual spatial resolution independence of the solutions reported in the article. The computational costs of the method in both 2D and 3D frameworks are reported in Appendix B.

3. Extension of the Kurtulus Modes

In the present section, the Modes defined in Kurtulus (2016) are considered for the flow past a NACA0010 airfoil. A wide number of numerical simulations, spanning from 0° to 90°, were carried out. Since in the range 26° – 30° numerous bifurcations of the solution have been detected, small variations of the incidence ($\Delta\alpha = 0.1°$) were adopted within it.

In Kurtulus (2016) only five Modes were defined, here this classification is extended in order to be more consistent with the different bifurcation branches of the solution. For the sake of clearness, the labels adopted in the present work are similar to the Kurtulus (2016) ones for all Modes but for the Mode III, which is indeed subdivided in four sub-cases: $a, b, c, a/c$.

The analysis on the different Modes is performed through:

- ⋄ the behaviours of the vorticity far field for describing the wake arrangements of the flow;
- ⋄ time series of the drag and lift forces highlighting how each Mode presents a typical time evolution;
- ⋄ the Fourier analysis of the lift force with the aim of showing period doubling phenomena up to fully chaotic regimes;
- ⋄ the orbits in the phase portrait diagram constructed considering the plane C_l-$\dot{C}_l$, again to detect the passages from regular to fully chaotic dynamics;

The force coefficients adopted for the analysis are defined as:

$$C_d := \frac{D}{{}^1\!/_2 \rho\, U^2\, c\, l}, \qquad C_l := \frac{L}{{}^1\!/_2 \rho\, U^2\, c\, l}. \tag{4}$$

where D and L are respectively the drag and lift forces, U the modulus of the free-stream velocity, c is the chord length of the airfoil and l is the airfoil span (l is set equal to 1 in a two-dimensional framework). The Reynolds number is defined as $\mathrm{Re} = \rho U c/\mu$ (with ρ the density and μ the dynamic viscosity) and it is set to 1000 throughout the present work. In order to avoid the onset of hysteresis phenomena, all the simulations are performed by starting from rest conditions.

Regarding the Fourier analysis, when a periodic regime is attained after the initial transition stage, the Fourier transform is performed within a time window where the signal may be assumed periodic. Conversely, when the signal is completely chaotic, the final time of the simulations is doubled and a wider time-window is chosen for the spectral analysis.

The definition of the phase space variables can be performed in different ways; in particular we followed Khalid and Akhtar (2012) and Nayfeh and Balachandran (2008), choosing the lift and its time derivative. Indeed, the lift force is strictly connected with the circulation distribution over the airfoil (see *e.g.* Saffman (1992)) which, for the Stokes' theorem, is equal to the integral of the vorticity field

over the fluid domain. Therefore, since we showed that the different Modes induce significant changes on the wake topology, we expect that also the lift force should be subjected to relevant modifications when passing from a Mode to another.

3.1. ■ *Mode I:* Continuous vortex sheet Mode, $\alpha \in [0° - 9°[$

As sketched in the figure (1), in the Mode I the vorticity field is characterized by two stable shear layers. On the suction side of the airfoil the vorticity is always negative, whereas on the pressure side it remains always positive. The flow around the airfoil is attached or it is characterized by a stable and narrow recirculation bubble near the trailing edge. The wake remains stable, Kelvin-Helmholtz instability is not present or develops only in the far-field without any detectable influence on the global force acting on the airfoil. As a consequence,

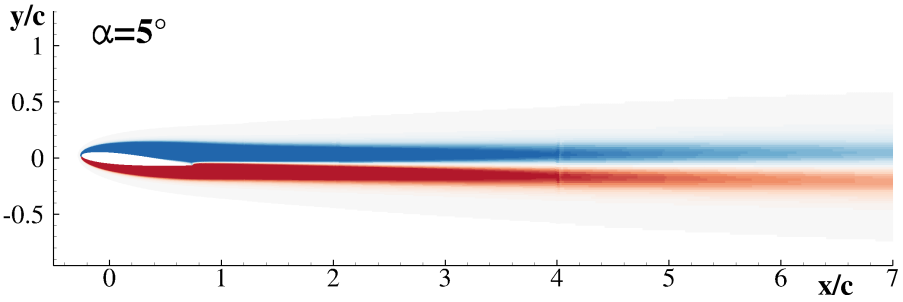

Figure 1: Wakes at angles of attack falling in the Mode I regime ■, computed at non-dimensional time $tU/c = 100$. Dimensionless vorticity $\omega c/U$ scales from -2 (blue) to 2 (red).

after a transient regime, both lift and drag forces reach a steady condition (see figure 2). Being the shedding mechanism not present yet and the force time signals

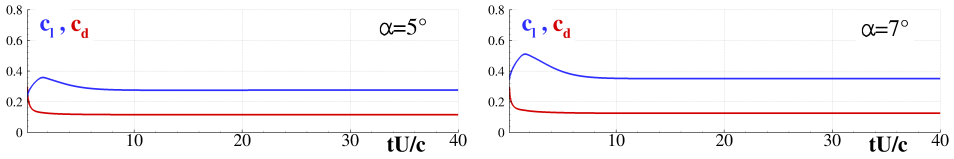

Figure 2: Time histories of the coefficients C_l and C_d at angles of attack falling in the Mode I regime ■.

practically constant, a spectral analysis as well as the description in terms of the phase-portrait diagrams are not performed.

3.2. ▲ *Mode II:* Alternating vortex shedding Mode, $\alpha \in [9° - 23°[$

When the airfoil enters in the Mode II regime, the shear layers in the far-field become unstable and the onset of the Von Kármán vortex shedding is already visible for the lower AoA falling in this Mode (*i.e.* $\alpha = 9°$). In terms of the dynamics of the shear layers, at $\alpha = 9°$, they are very stable and no separation is observed. Downstream of the airfoil, the shear layers organize in vortex patches of elongated shape and opposite circulation sign. Just after the near-field, a poor mutual interaction of the vorticity patches is observed and the axisymmetrization (described in Melander et al. (1987)) induces the filamentation. The filaments are then rapidly diffused.

As the AoA grows, the flow separates on the suction side and the upper shear layer tends to roll-up with the local formation of a "λ-shaped" vorticity structure (see Durante et al. (2016)). By increasing the angle of attack up to the stall inception, Kelvin-Helmholtz instability grows in intensity and the vorticity pattern becomes more complex, with a violent strain of the vortex cores and with the rearrangement in dipoles (see the case at $\alpha = 22°$). As shown in the third frame of figure (3), at $\alpha = 20°$ the positive and negative vorticity patches in the wake tend to rotate their dipole-axes and to organize in the far field in an aligned fashion. At $\alpha = 22°$ a local reattachment follows the initial separation on the suction side, while on the pressure side the lower shear layer suddenly wraps behind the trailing edge. In this last AoA falling within this Mode, the wake arrangement changes and the dipoles strongly interact each-other, inducing a more complex vorticity pattern in the far wake.

As shown in figure (4), the instability in the shear layers at 9° and 10° causes small amplitude oscillations on the forces which widen until $\alpha = 17°$. Starting from $\alpha = 13°$, the lift signal departs from a pure sinusoidal one and at $\alpha = 22°$ small sub-harmonics are observed. It is worth to underline that, from $\alpha = 20°$, the airfoil is in a stall condition and the lift derivative with the incidence, $dC_l/d\alpha$, reduces to zero (see also section 5).

When the angle of attack is low (*i. e.* 9°, 10°) the spectra show an isolated peak correspondent to the shedding frequency. By increasing the incidence, the number of frequency peaks (and their intensity) grows, as visible by comparing the top left and the bottom right plots of figure (5). For the angle $\alpha = 22°$, the lift spectrum presents four isolated and more energetic peaks as well as four lower ones, thus indicating a period doubling mechanism inception, similarly to what found by Pulliam and Vastano (1993) and Rossi et al. (2018) when the Reynolds number is gradually increased. The dominant frequency for $\alpha = 22°$ attains at $fU/c \approx 0.46$.

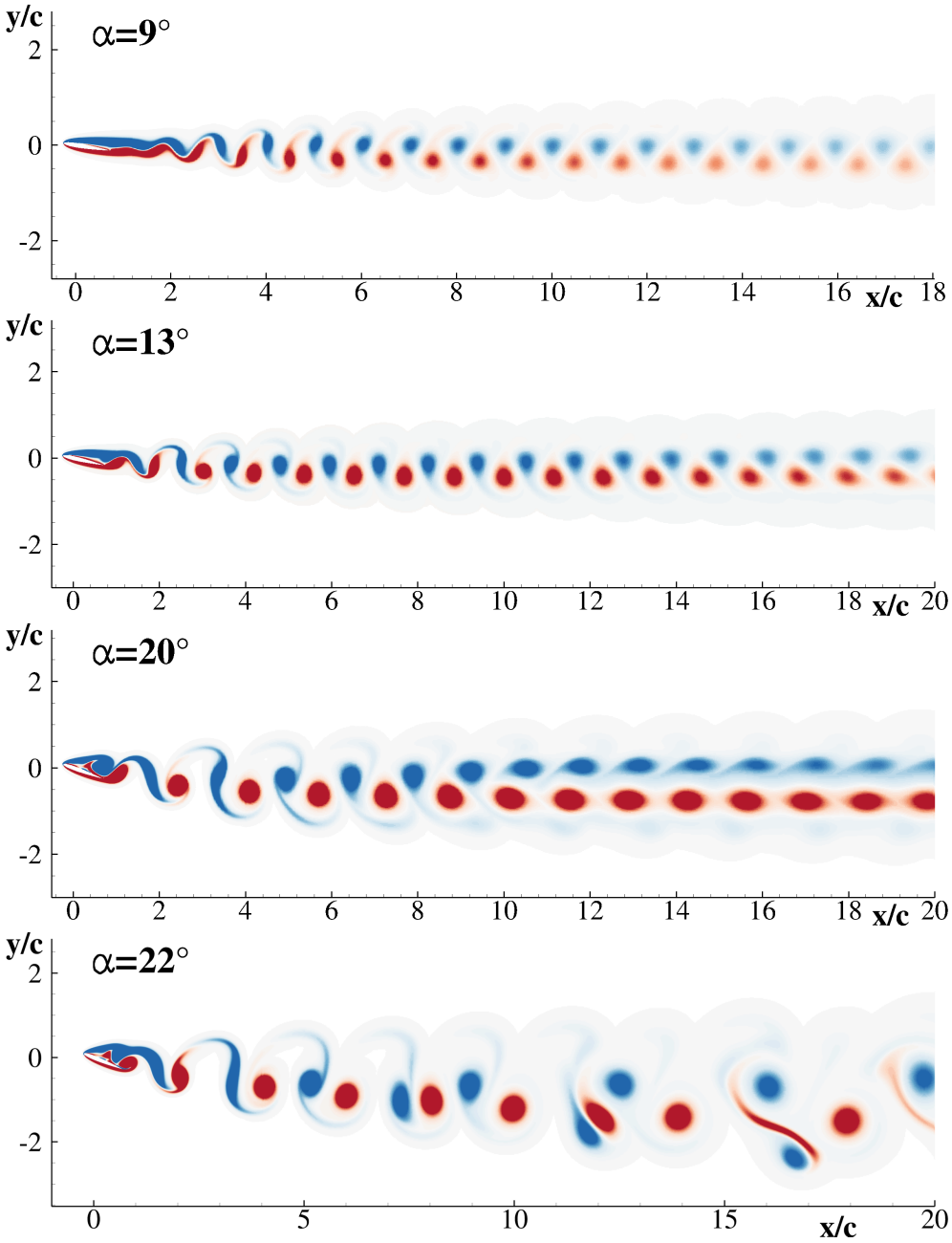

Figure 3: Wakes at angles of attack falling in the Mode II regime ▲, computed at non-dimensional time $tU/c = 100$. Dimensionless vorticity $\omega c/U$ scales from -2 (blue) to 2 (red).

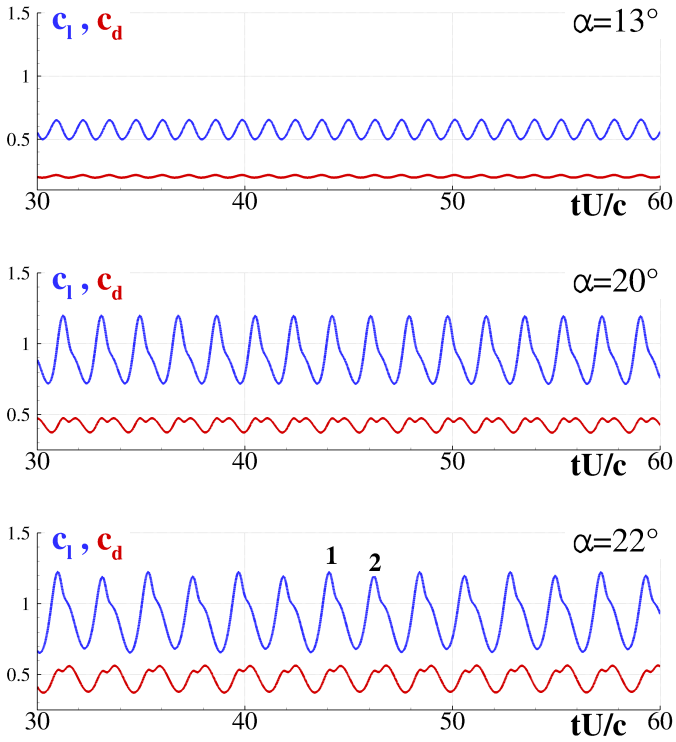

Figure 4: Time histories of the coefficients C_l and C_d at angles of attack falling in the Mode II regime ▲.

By looking at figure (6), the periodic behavior of the time signals corresponds to closed curve orbits in the phase portrait diagrams. Up to 13° the signals are almost monochromatic, so that the orbits are almost elliptical. When the angle of attack rises, the orbits start to deform more and more assuming a "bean like" shape (see the case $\alpha = 20°$). At $\alpha = 22°$ the phase portrait diagram exhibits two stable orbits very similar and very close to each other.

The map on figure (6) are clockwise oriented and the intersections of the orbit with the axis $\dot{C}_l = 0$ is marked with red dots when the lift forces present a local maximum. Those dots represent the Poincarè sections. Remarkably, two dots appear in the Phase portrait diagram at $\alpha = 22°$ highlighting a doubling-period bifurcation.

3.3. ◄ *Mode IIIa:* shedding of two distinct vortex pairs, $\alpha \in [23° - 26.5°[$

Starting from $\alpha = 23°$, the wake reorganizes in a new configuration: a straight alignment of dipoles pointing downward is surmounted by more intense dipoles

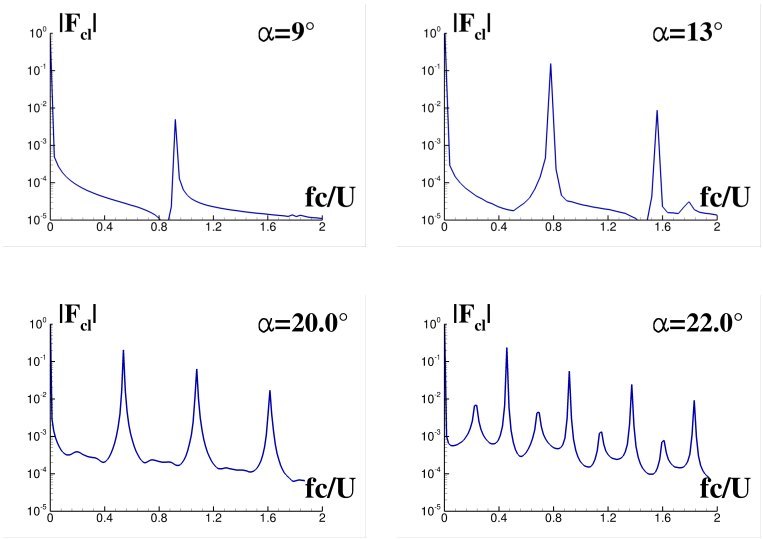

Figure 5: Fourier Spectra of Lift time signals for different angles of attack falling in Mode II regime ▲

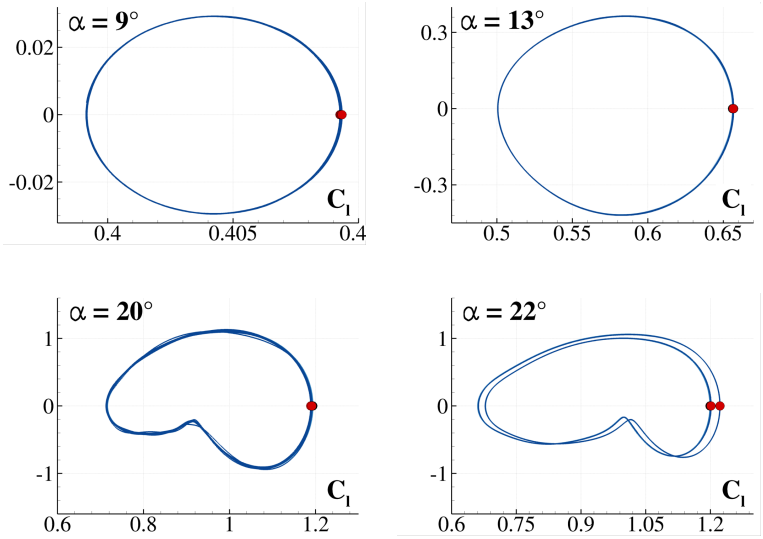

Figure 6: Phase portrait diagram C_l-$\dot{C}_l$ from the cases falling in Mode II regime ▲. Red bullets correspond to the Poincarè sections.

pitched up and bent over counter-clockwise. Increasing the angle of attack, the uprising dipoles increase their vertical velocity enlarging the wake width and moving even more clockwise. At $\alpha = 25°$ the dipoles are completely bent

streamwise, whereas from $\alpha = 26°$, the more they move away from the profile, the more their axes rotate, transversally intersecting the wake and eventually interacting with the straight-aligned dipoles. As a consequence, the vorticity pattern in the far-field becomes more intricate and approaches to a chaotic condition.

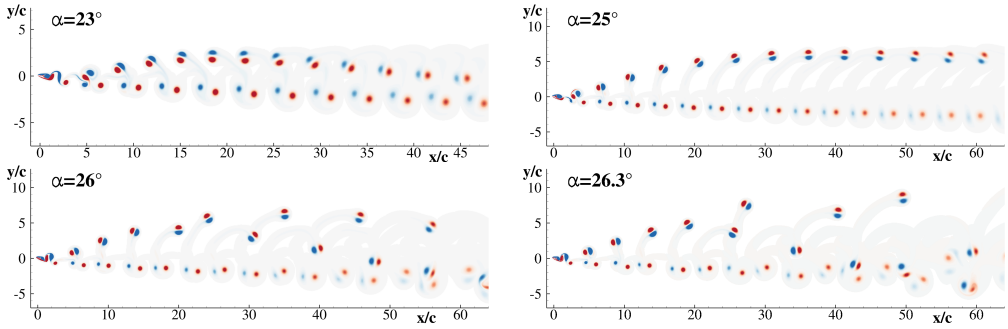

Figure 7: Wakes at angles of attack falling in the MODE IIIa regime ◀, computed at non-dimensional time $tU/c = 100$. Dimensionless vorticity $\omega c/U$ scales from -2 (blue) to 2 (red).

From $\alpha = 23°$ the Mode IIIa starts and intense sub-harmonic modulations are visible when looking at the lift plots in figure (8). The amplitude of these sub-harmonics increases with α. After the transient stage, the lift signal reaches a periodic behaviour where a dominant peak is followed by two lower ones.

With respect to the spectral analysis in figure (9), at $\alpha = 23°$ the dominant frequency remains almost unchanged (growing actually of about the 1%), even though the peak intensity lowers from 0.237 to 0.207, while the intensities of the other frequency components are increasing. The same features are shared with $\alpha = 24°$ and $\alpha = 25°$ whereas the spectrum at $\alpha = 26°$ shows a clear doubling-period bifurcation respect to the previous cases similarly to what shown for the case $\alpha = 22°$ in the previous subsection. The mechanism is perceivable also in the wake rearrangement shown in figure (7), where the wake at $\alpha = 26°$ presents a more irregular vorticity field. For $\alpha = 26.3°$ and $\alpha = 26.4°$ the time signal of the lift force is characterized by 12 local maxima in a period, thus showing a further bifurcation with a doubling period with respect to $\alpha = 26°$. From the spectral analysis, shown in figure (9), the number of peaks passes from 16 at $\alpha = 26°$ to 32 at $\alpha = 26.3°$.

When considering the phase portrait diagrams in figure 10 it is patently clear that $\alpha = 23°$ and $\alpha = 25°$ are characterized by three concatenate loops corresponding with three points in the Poincarè section. In particular the leftward

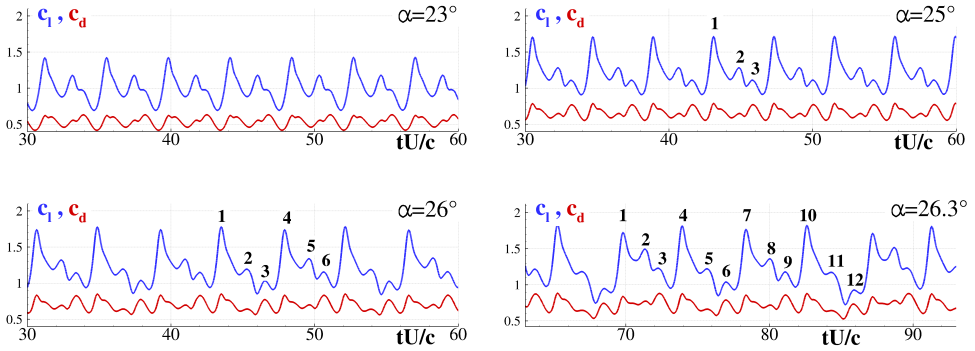

Figure 8: Time histories of the coefficients C_l and C_d at angles of attack falling in the Mode IIIa regime ◄.

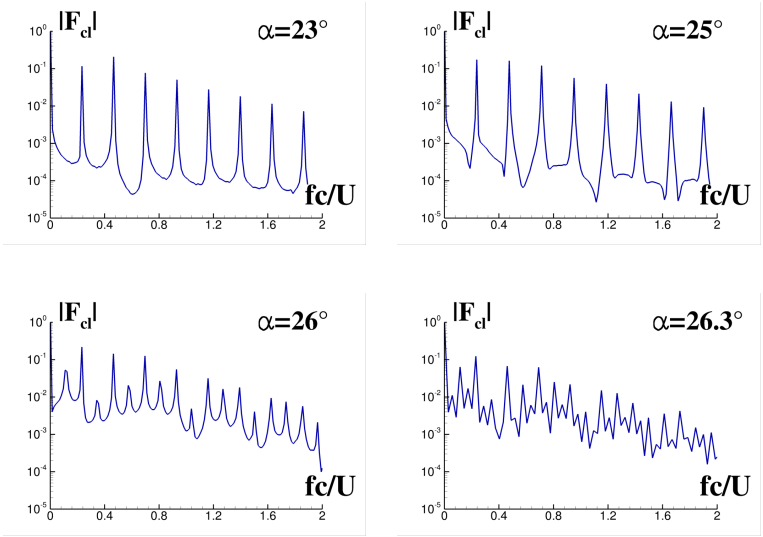

Figure 9: Fourier Spectra of Lift time signals for different angles of attack falling in Mode IIIa regime ◄

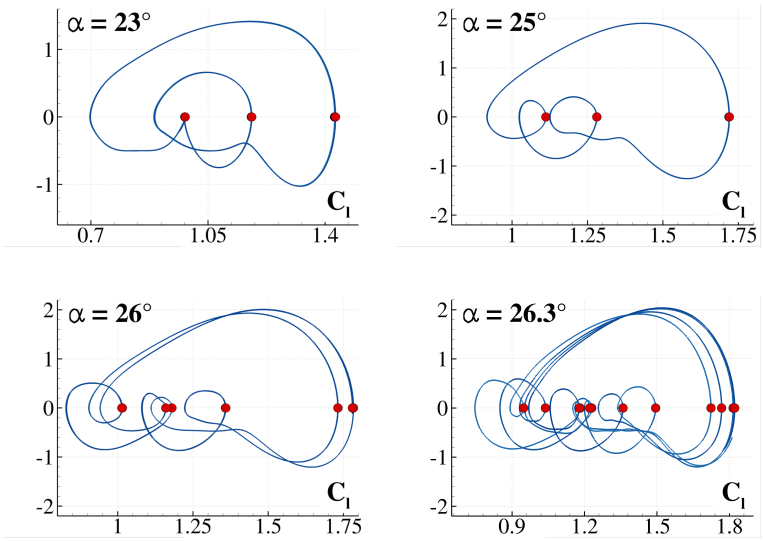

Figure 10: Phase portrait diagram C_l-$\dot{C}_l$ from the cases falling in Mode IIIa regime ◂. Red bullets correspond to the Poincarè sections

loop is increasing in size while the middle one is reducing. The presence of three points in the Poincarè sections is associated with a tripling period (three local maxima in one period of the lift signal).

At $\alpha = 26°$ the solution bifurcates with the doubling of the orbits and the consequent appearance of six points in the Poincarè section. This is a doubling bifurcation of the former tripling period. For this case six local maxima are present in one period of the lift signal (see center-right plot of figure (8)).

At $\alpha = 26.3°$ and $\alpha = 26.4°$ the solution bifurcates again as stressed before and twelve points in the Poincarè section appear in the phase portrait diagrams.

The phenomena discussed in this section prelude to the chaotic cascade which will be discussed in the next subsection. To the authors knowledge this mechanism linked to the tripling period has never been observed in the present literature.

3.4. × *Mode III a/c:* chaotic shedding behavior, $\alpha \in [26.5° - 27.1°[$

By further increasing the incidence the wake becomes completely chaotic, as shown in figure (11). This is due to the fact that each uprising dipole presents an angular velocity of its axis with a sign and an intensity that changes unpredictably. The mutual interaction of these dipoles produces a chaotic vorticity pattern. This dynamic behavior of this latter resembles the chaotic one of two interacting dipoles with different circulations, discussed in Riccardi and Durante (2006). The

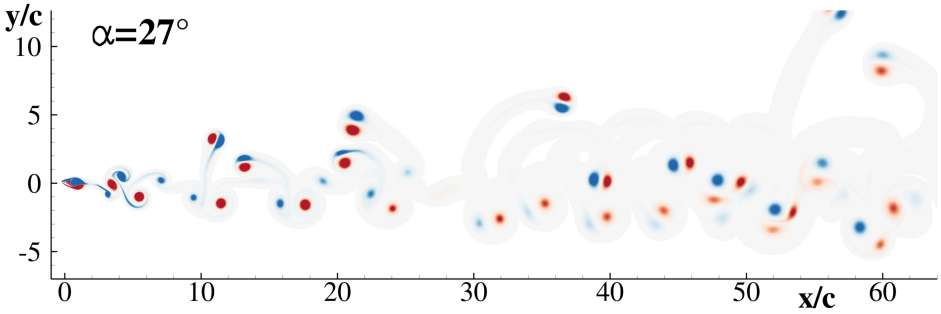

Figure 11: Wake at angle of attack falling in the MODE IIIa/c chaotic regime ×, computed at non-dimensional time $tU/c = 100$. Dimensionless vorticity $\omega c/U$ scales from -2 (blue) to 2 (red).

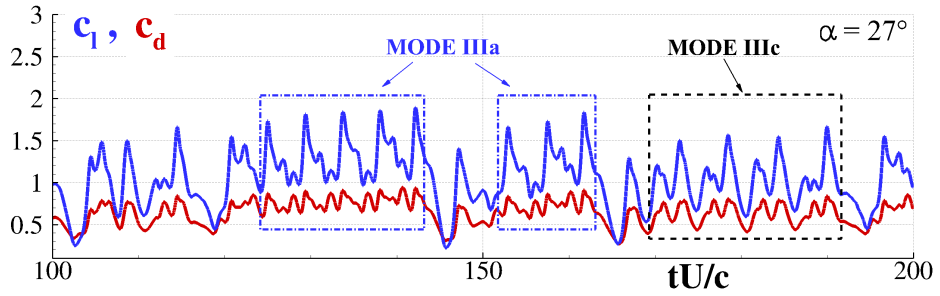

Figure 12: Identification in the time histories of force coefficients of Mode IIIa (◂) and Mode IIIc (▾) patterns at Mode IIIa/c (×) case $\alpha = 27°$.

irregularities of the vorticity patterns of the Mode IIIa/c reflect those one of the time histories of the forces shown in figure (12). In this plot an alternating of the IIIa and IIIc Mode patterns is observed and evidenced with boxes. The first one is related to the Mode IIIa, while the second is linked to the Mode IIIc. This trend results from a bifurcation in time of the solution between Mode IIIa and Mode IIIc. This aspect helps to understand that the chaotic nature of the vorticity in the wake comes from an alternate shedding of vortex dipoles arranged as in the Modes IIIa and IIIc, the constant interaction of which gives as a result a messy arrangement of the vorticity field. Since a stable scenario was never observed, we preferred to classify this Mode as chaotic and the symbol × has been associated with it. For this specific regime, the final time of the simulations has been shifted up to $200c/U$ seconds in order to check whether a stabilization of the solution (representing a new Mode) was recognized.

The frequency behaviour seen in the former regime drastically changes in the Mode IIIa/c because of its chaotic nature. Top plots of figure (13) show an

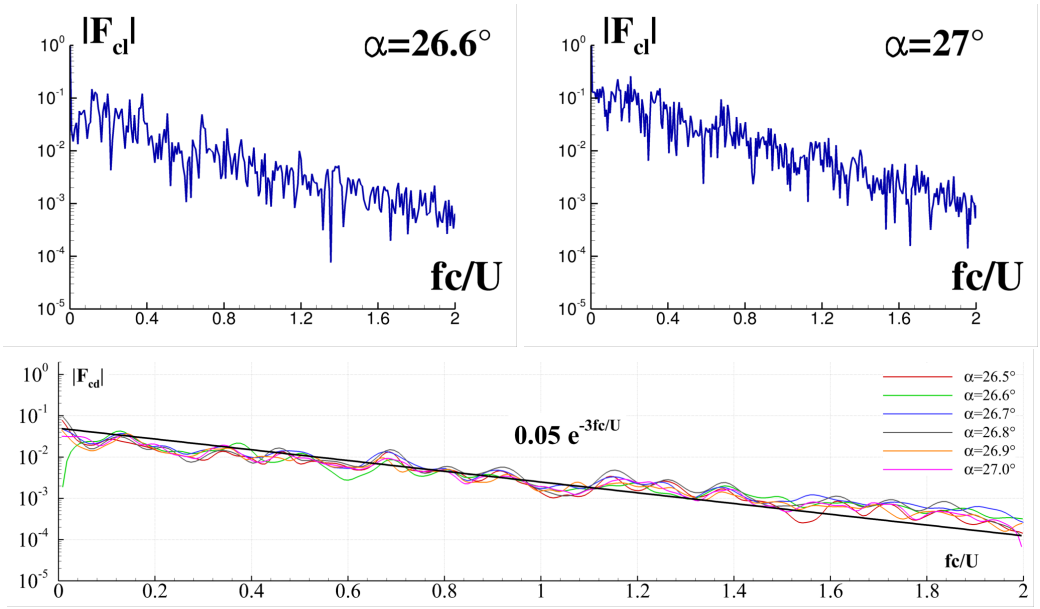

Figure 13: Top: Fourier Spectrum of Lift time signals for angle of attack falling in Mode IIIa/c regime ×. Bottom: filtered spectra of C_d falling in the same regime and global exponential behaviour.

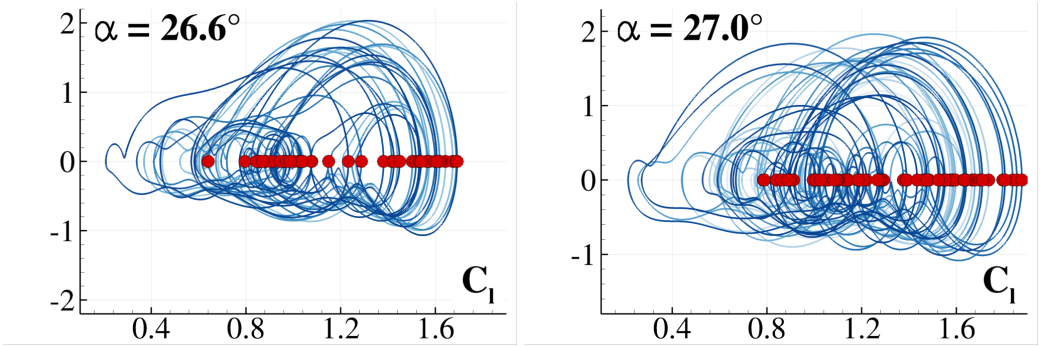

Figure 14: Phase portrait diagram C_l-$\dot{C}_l$ from the cases falling in Mode IIIa/c regime ×. Red bullets correspond to the Poincarè sections

almost continuous spectrum of the lift force. The bottom plot of the same figure depicts the smoothed spectra for different AoA. Remarkably, the steepness of all the smoothed spectra show a similar trend, with a frequency decay slope of -3 (*i.e.* close to the function $\exp(-3fU/c)$).

As remarked in Durante et al. (2016), the time variation of the kinetic energy

and the drag force are connected to the enstrophy according to equation:

$$\frac{d\varepsilon_K}{dt} = F_D U - 2\mu E(\omega)\,, \qquad E(\omega) := \frac{1}{2}\int_\Omega \omega^2 dV \tag{5}$$

where F_D is the modulus of the drag force, ε_K is the total kinetic energy and $E(\omega)$ represents the total enstrophy.

The variation of the kinetic energy tends to become negligible in a time averaged sense when the system reaches a period regime, so that, the spectral distribution of the drag modulus and of enstrophy should be similar. Consequently, since the direct cascade of enstrophy in 2D flow is known to have a slope of -3, the same holds for the spectrum of the drag forces as shown in figure 13.

When passing to Mode IIIa/c regime, the chaos inception is also reflected in the phase portrait diagrams of figure (14) where numerous orbits are a direct consequence of the impossibility for the system to find a stable limit cycle.

3.5. ▼ *Mode IIIc:* from a chaotic to a compact wake pattern shedding, $\alpha \in [27.1° - 28.5°[$

From the chaotic behavior seen in the Mode IIIa/c, a little increasing of the AoA to $\alpha = 27.1°$ makes the vorticity pattern turn back to a more organized structure.

From the top plot of figure (15), it is possible to appreciate that the uprising dipoles are still present, although their number is significantly reduced. As the AoA grows, the vertical velocity of these latter gradually reduces and in the cases $\alpha = 28°$, $\alpha = 28.3°$ and $\alpha = 28.4°$ the uprising mechanism is absent, making the wake even more compact (see figure (15)).

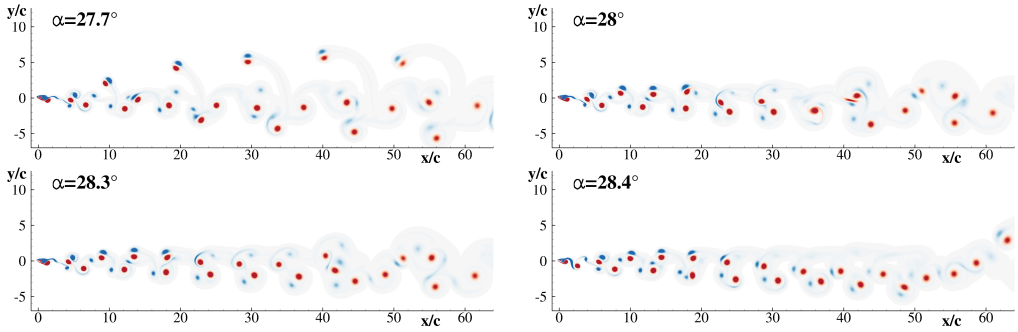

Figure 15: Wakes at angles of attack falling in the MODE IIIc regime ▼, computed at non-dimensional time $tU/c = 100$. Dimensionless vorticity $\omega c/U$ scales from -2 (blue) to 2 (red).

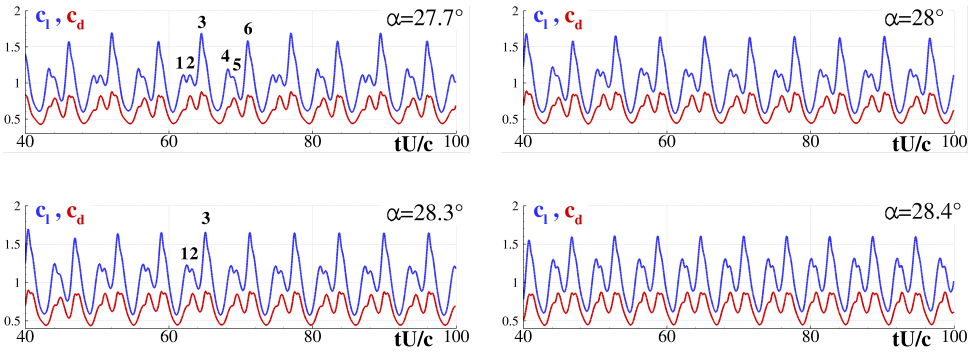

Figure 16: Time histories of the coefficients C_l and C_d at angles of attack falling in the Mode IIIc regime ▼.

Although the wake arrangement radically changes within the present range of angle of attack, the time signals of the lift and drag coefficients recover an evident regularity and the mean values of the forces appear slightly affected by the AoA, remaining almost constant (see figure (16)). With respect to the previous cases, this Mode needs longer transients in order to get stable solutions. For example a stable condition is achieved around $tU/c = 40$ for the cases shown. The lift signals are now characterized by a dominant peak preceded by two lower ones.

However, all the cases falling within this Mode, although stable, cannot be classified as strictly periodic since small differences appear from one cycle to another. As a consequence, the spectrum recasts again in a "discrete peaks" fashion whereas, rising the AoA, the number of frequency peaks reduces with an inverse cascade mechanism, as shown in figure (17). In particular, for $\alpha = 27.7°$ twenty-four well distinguishable peaks can be recognized within the frequency range $fc/U \in (0, 2]$ while for $\alpha = 28.4°$ twelve peaks are present in the same range. The above results represent an halving route from the previous chaotic regime, never discussed before in literature as far as the authors' knowledge.

On the phase portrait diagrams multiple orbits are still visible at $\alpha = 27.1°$ and $\alpha = 27.6°$, although more clustered compared to the chaotic cases. Moving toward higher angles of attack, at $\alpha = 27.7°$ a double orbit with concatenate loops appears with six points in the Poincarè section which correspond to six local maxima in a period highlighted in the related plot in figure (16). At $\alpha = 28.3°$ and $\alpha = 28.4°$ one single orbit appears with two concatenate loops similarly to what shown for the Mode IIIa. As in the latter three local maxima on the lift signal in a period are present, *i.e.* tripling-period (figure (16)).

In conclusion, in the same way in which the Mode IIIa represents a *direct route*

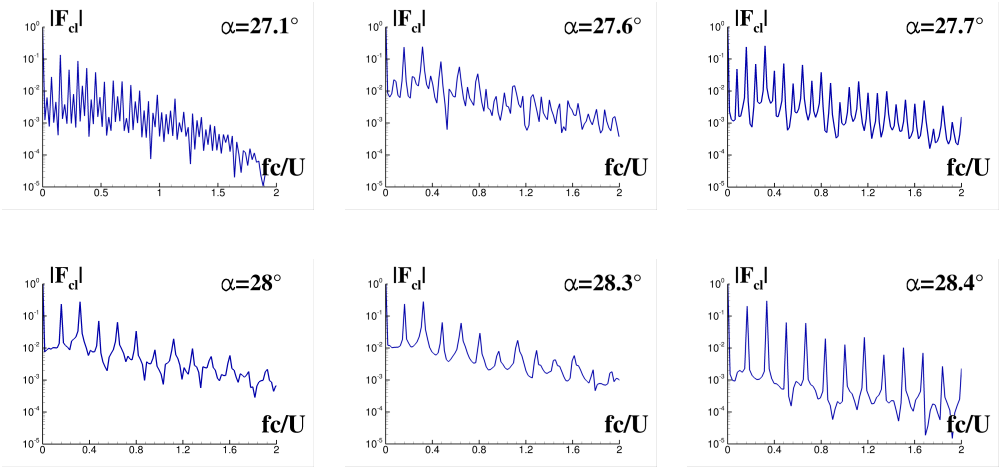

Figure 17: Fourier Spectra of Lift time signals for different angles of attack falling in Mode IIIc regime ▼

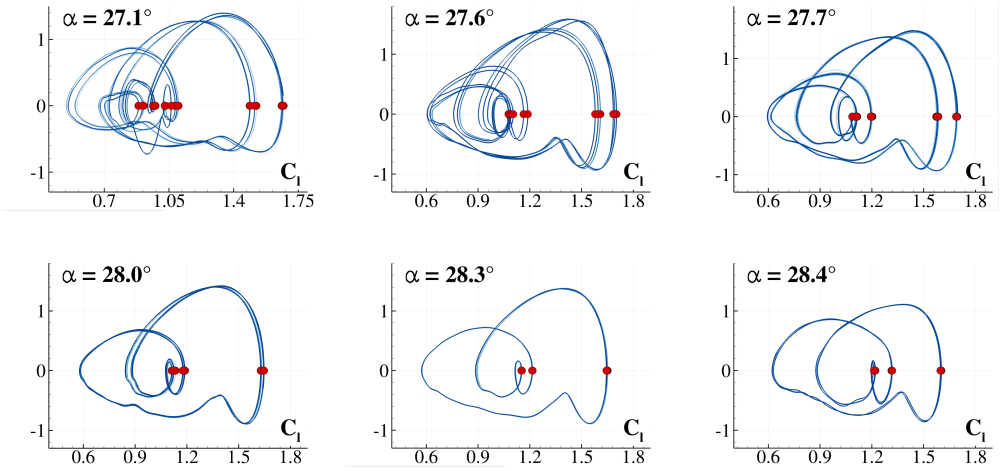

Figure 18: Phase portrait diagram C_l-$\dot{C}_l$ from the cases falling in Mode IIIc regime ▼. Red bullets correspond to the Poincarè sections.

to chaos, the Mode IIIc represents the inverse behavior with a *reverse route from chaos*.

3.6. ▶ *Mode IIIb and* ◆ *Mode IV:* bifurcation between two stable Modes, $\alpha \in [28.5° - 44°[$

After the Mode IIIc, the region where the Mode IIIb and the Mode IV coexist appears from $\alpha = 28.5°$. The Modes IIIb and IV are always associated one to another and, therefore, we prefer to treat them together. In the Mode IIIb the wake structure resembles the Mode IIIa. However, within this regime the uprising dipoles are more intense to the detriment of the lower aligned ones. As sketched in figure (19), the intensity of the uprising dipoles grows with the increasing incidence.

Conversely, the Mode IV is distinguishable by a narrow wake with a peculiar vorticity distribution, characterized by two different sets of vortices: the lower set is formed again by dipoles, while the upper one by a row of clockwise vortex patches (see figure (20)). As discussed below, this vorticity pattern is associated with a regular and almost monochromatic time behavior of the lift force.

It is worth to note that the Mode IV resembles the Mode **P+S** (one pair and one single vortex shed in one period) of the flow past a forced oscillating circular cylinder, which was observed through the experimental dye visualizations (see Williamson and Govardhan (2004)). Conversely, the Mode IIIb resembles the one

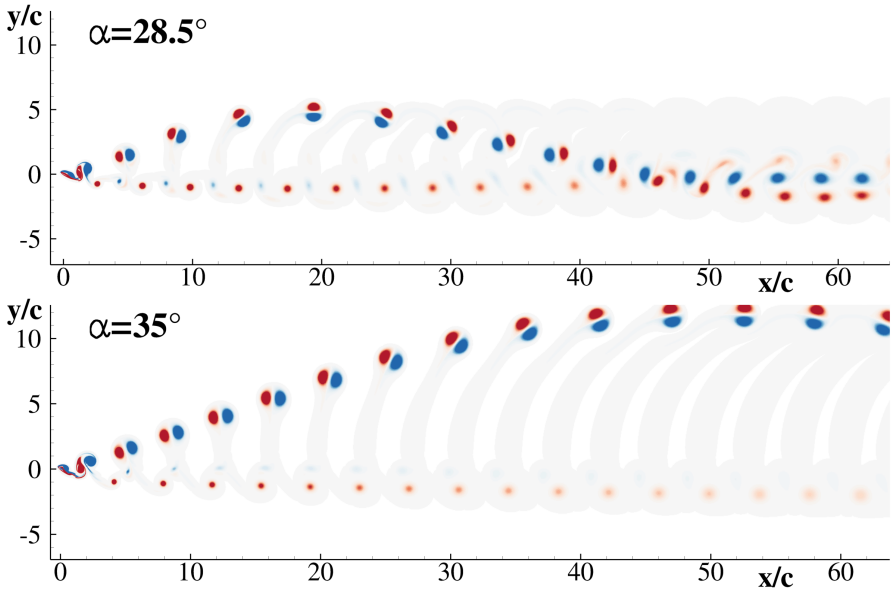

Figure 19: Wakes at two angles of attack falling in the Mode IIIb ▶, computed at non-dimensional time $tU/c = 100$. Dimensionless vorticity $\omega c/U$ scales from -2 (blue) to 2 (red).

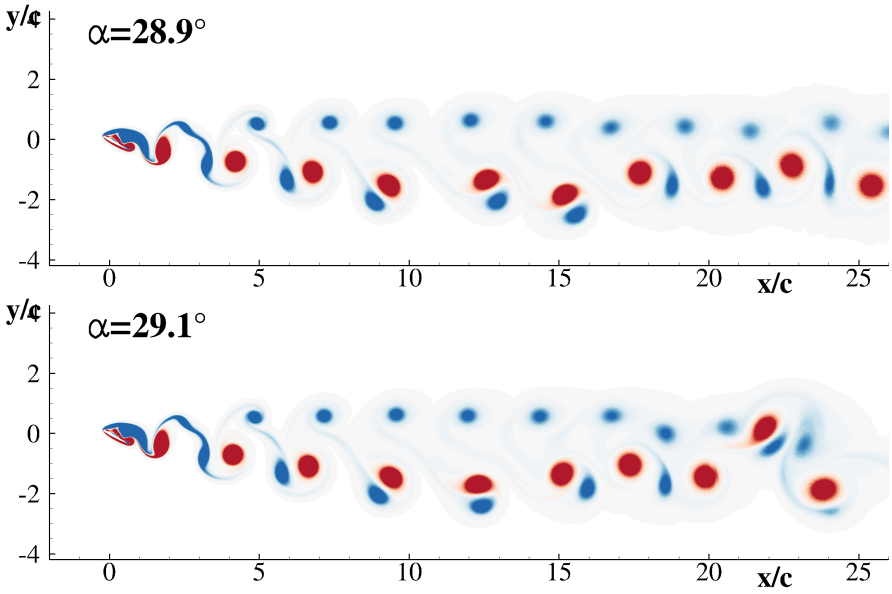

Figure 20: Wake at angles of attack $\alpha = 28.9°$ and $\alpha = 29.1°$ falling in the Mode IV regime ◆, computed at non-dimensional time $tU/c = 116$. Dimensionless vorticity $\omega c/U$ scales from -2 (blue) to 2 (red).

found experimentally and numerically by Jones et al. (1998) for a plunging airfoil and numerically investigated by Badrinath et al. (2017) recently.

From 28.5° the Mode IIIb begins with abrupt variations of the mean values of the forces with respect to the former Mode (see figures (16 and (21). In the range $28.5° - 29.3°$, the solution bifurcates between Mode IIIb and Mode IV. After that range, only the Mode IIIb holds on until $\alpha = 43°$.

For the sake of clearness, in figure (21) only forces time histories of Mode IIIb cases have been collected, whereas the time evolution of Mode IV cases are not shown. The Mode IV exists only within a narrow interval of AoA, which was already identified by Kurtulus (2016). However, in that work a NACA0002 airfoil was considered and a wider range was detected, thus indicating that the airfoil thickness significantly influences the persistence of the Mode IV. Among the differences between the two regimes, it appears that the transient stages are longer for the Mode IV than the Mode IIIb. The sub-harmonics seem to gradually disappear when entering in the Mode IV, thus recasting the periodic regime signal to an almost monochromatic one. More specifically, the Mode IIIb, for $\alpha = 28.5°$ and $\alpha = 35°$ the time behaviors shown in figure (21) are highly regular with a sequence of three lift local maxima in the period. Figure (22) depicts the spectra

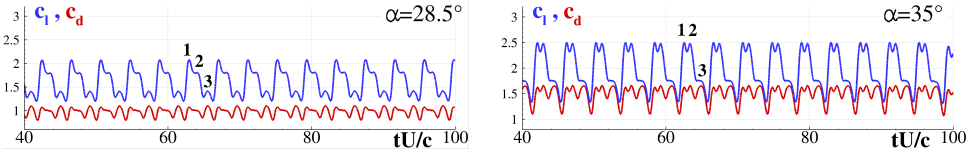

Figure 21: Time histories of the coefficients C_l and C_d at angles of attack falling in the Mode IIIb regime ▶.

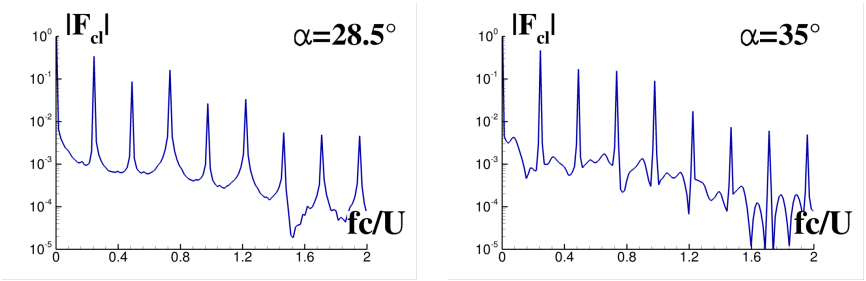

Figure 22: Fourier Spectra of Lift time signals for different angles of attack falling in Mode IIIb regime ▶

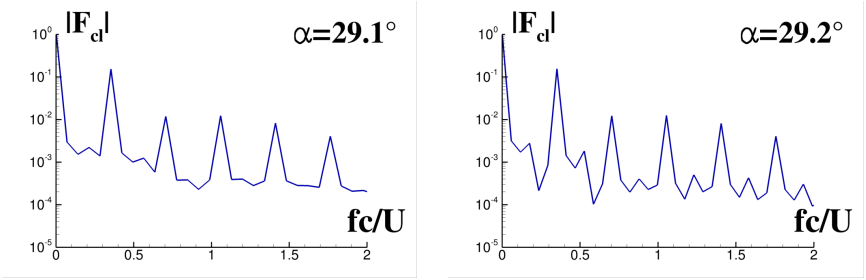

Figure 23: Fourier Spectra of Lift time signals for different angles of attack falling in Mode IV regime ◆

for the Mode IIIb which are characterized by 8 frequency peaks. This is consistent with the strong analogy between Mode IIIa and Mode IIIb which share similar wake patterns. When passing from Mode IIIb to Mode IV, the solution bifurcates and the number of dominant frequencies passes from 8 to 5, as shown in figure (23). Therefore, by increasing the angle of attack, a further bifurcation occurs when the dynamical system comes back to the Mode IIIb from the Mode IV. From the Mode IV spectra it should be noticed that the dominant frequency presents an intensity larger than the other threes, indeed, an almost monochromatic time behavior of the forces is identified.

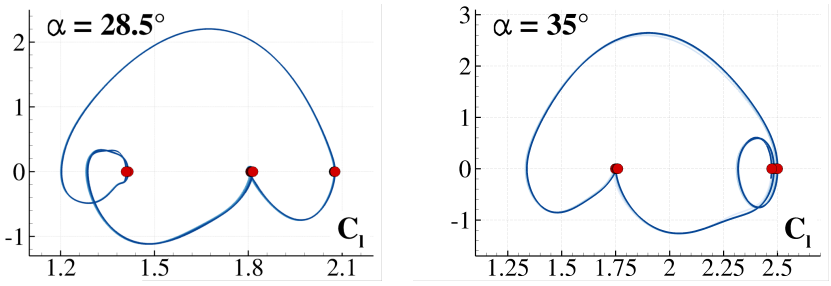

Figure 24: Phase portrait diagram C_l-$\dot{C}_l$ from the cases falling in Mode IIIb regime ▶. Red bullets correspond to the Poincarè sections.

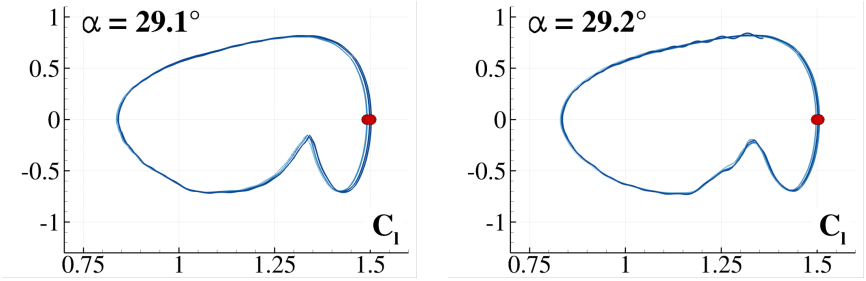

Figure 25: Phase portrait diagram C_l-$\dot{C}_l$ from the cases falling in Mode IV regime ◆. Red bullets correspond to the Poincarè sections.

Figure (24) refers to phase portrait diagram for the Mode IIIb which exhibits a double-knotted orbit in the map, indicating a tripling-period regime. Passing from $\alpha = 28.5°$ to $\alpha = 35°$ the two higher local maxima of the lift become closer. Conversely, within the Mode IV a single orbit takes place, being the spectra characterized by a singular dominant frequency (see figure (25)).

Increasing the AoA beyond $\alpha = 29.2°$ the Mode IV disappears and only Mode IIIb exists. In the range $\alpha \in [30, 44)$ the Mode IIIb presents irregularities in the solution and the number of local maxima increases or shrinks, but this behavior is nor here further discussed for the sake of conciseness.

3.7. ● *Mode V:* Bluff body vortex shedding Mode, $\alpha \in [44° - 90°]$

When α exceeds the 43°, the wake assumes the typical characteristics of the shedding around a bluff body. In this case, two patches of vorticity are uniformly released by the upper and lower part of the body. The results at $\alpha = 90°$ are in good agreement with Najjar and Vanka (1995), where the flow past a vertical flat plate was investigated. The vorticity pattern of the Mode V follows the

same behaviour observed in this pioneering work and similar values of the drag coefficients (*i.e.* 3.5 versus the present 2.95) where also recovered, although the effect of the thickness plays a non trivial role in lowering this quantity, as remarked by Tian et al. (2011).

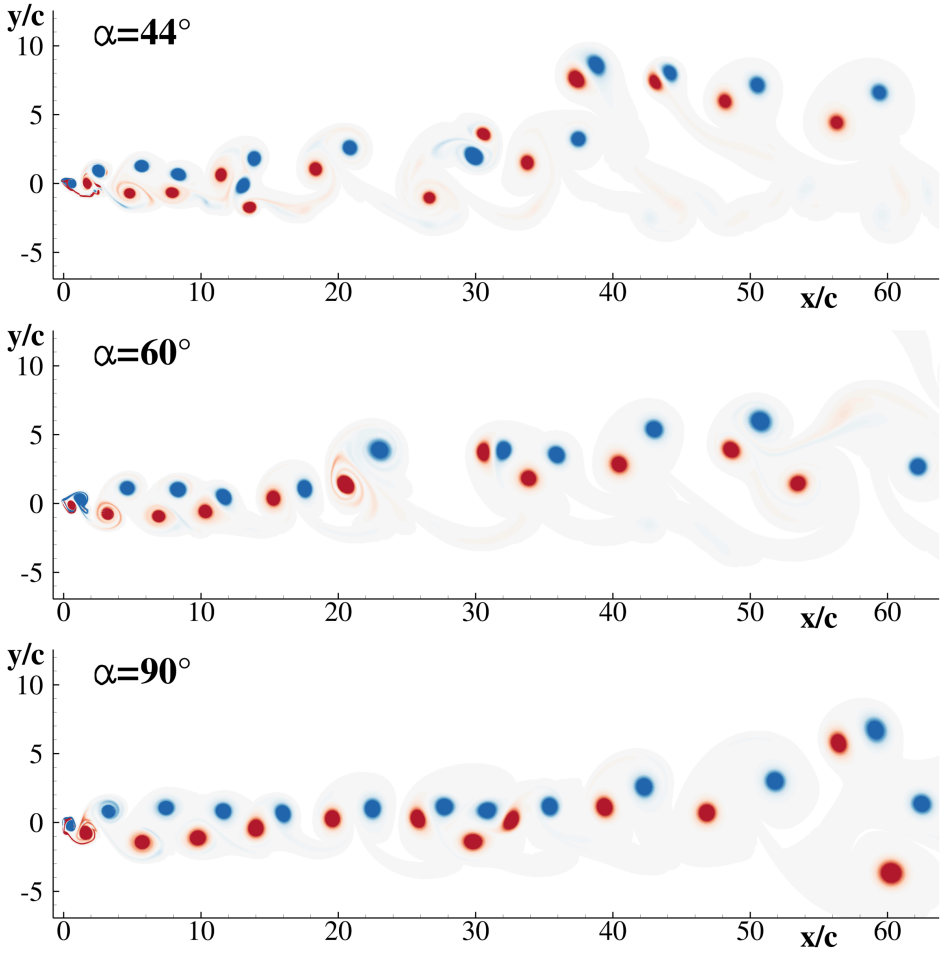

Figure 26: Wakes at angles of attack falling in the Mode V regime ●, computed at non-dimensional time $tU/c = 100$. Dimensionless vorticity $\omega c/U$ scales from -2 (blue) to 2 (red).

The Mode V starts when the angle of attack exceeds the 43°. At $\alpha = 45°$, as expected, the lift mean value equals the drag one, while it lowers for higher angles, becoming the drag dominant. In this case the airfoil behaves like a bluff body and the lift force time signal at $\alpha = 90°$ resembles a monochromatic wave oscillating around a zero value.

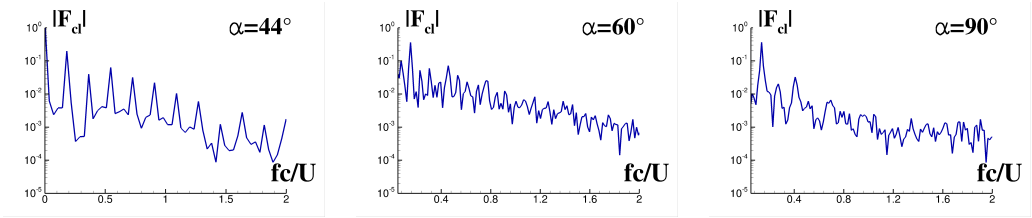

Figure 27: Fourier Spectra of Lift time signals for different angles of attack falling in Mode V regime ●

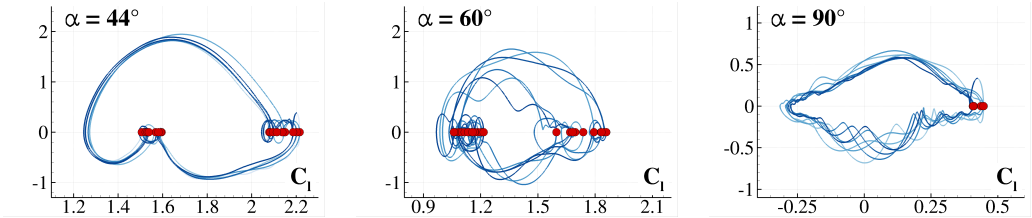

Figure 28: Phase portrait diagram C_l-$\dot{C}_l$ from the cases falling in Mode V regime ●. Red bullets correspond to the Poincarè sections.

Being this Mode related to the flow past a bluff body, it is expected that a single dominant frequency, corresponding to the shedding, should be distinguished in the spectrum. By looking at the figure (27), it is possible to see how, when the incidence grows, the system gradually assumes this expected behavior. The spectrum at $\alpha = 44°$ still presents numerous isolated peaks, but the situation abruptly changes as the angle of attack reaches $\alpha = 60°$: the spectrum now resembles the attended one, with an isolated peak which moves from 0.18 of $\alpha = 44°$ to 0.14 of $\alpha = 90°$. This is in agreement with the Strouhal number found by Najjar and Vanka (1995) for a vertical flat plate at Re=1000, St=0.132.

When the system enters in the Mode V regime the phase portrait diagrams move towards a single orbit dynamics which, however, presents evident irregularities linked to the complex vortex shedding mechanism, typical of the flow past a bluff body.

4. Discussion on the stability of the Modes

In the present section a general discussion on the stability of the dynamical system is addressed. Global and local approaches are used in order to evaluate it quantitatively. First of all the Poincarè sections shown above are collected

together in order to built a bifurcation diagram for the α parameter. This diagram shows how increasing the AoA the system develops the doubling, the tripling, the double-tripling, the quadrupling-tripling dynamics up to the chaotic behavior, and how the latter is confined in a region giving rise to an inverse cascade with halving period bifurcations where again a new tripling and pure monochromatic regimes develop for larger incidences.

Furthermore, the dominant Lyapunov exponents are calculated for every lift time history, according to the algorithm of Wolf et al. (1985). The Lyapunov exponent, λ_{Max}, of a dynamical system is a quantity characterizing the rate of separation of infinitesimally close trajectories, so that it represents a measure of the sensitivity of the system to become unstable under certain initial conditions. Positive values of the exponent may indicate an evolution of the system toward a chaotic behavior, although it does not represent a sufficient condition (see, for example, Leonov and Kuznetsov (2007)).

Traditionally, systems are recognized as chaotic when $\lambda_{\text{Max}} > 0$. However, with high-dimensional systems like fluid flows the exact calculation of λ_{Max} is rarely possible. The trends in $\lambda_{\text{Max}} > 0$ are still significant, where an increase in λ_{Max} is correlated with a decreased stability of the system and its dominant modes. These trends are shown here to correlate with the bifurcation patterns observed via other methods.

The section is concluded studying the response of a Mode to a severe perturbation of the upstream conditions. It will be shown that the Modes discussed in this work are quite stable, once the vorticity wake is developed, and even after a large perturbation the dynamical system falls again in the starting Mode.

4.1. General discussion on period-doubling, period-tripling and route to chaos

In figure (29) the local maxima of the lift force within the time windows selected for the Fourier transform are highlighted with symbols (similarly to ones used in Section 3). These points were already depicted as Poincarè sections in the phase portraits C_l-$\dot{C}_l$ of the former section (figures (6), (10), (14), (18), (24), (25), (28)), but they are collected together in order to show the bifurcations related to the incidence increment. Up to 10°, within the linear limit, the maxima are fitted to the mean curve whereas the dominant Lyapunov exponents are rather low (see figure (30)), thus indicating a stable behavior. In the range 22°-27° (magnified in the bottom frame of figure (29)) the bifurcations already discussed in sections 3.3 and 3.4 lead to a doubling-period at $\alpha = 22°$ (correspondent to the formation of two periodic orbits shown in figures (6)), a tripling in the range 23°-25°, and following bifurcations at $\alpha = 26°$ where 6 maxima appear. From

$\alpha \in [26.1°, 26.4°]$ twelve maxima appear indicating a further doubling-period mechanism. From $\alpha = 26.5$ to $\alpha = 27°$ the cascade to chaos take place with continuous bifurcations and increasing Lyapunov exponents (see bottom frame of figure (30)). Once the 27° are exceeded, two groups of maxima mark the passage to Mode IIIc and the inverse cascade mechanism which brings back to three the number of maxima for $\alpha \geq 28.2°$.

In the same interval the dominant Lyapunov exponents tend to lower with a marked stability between 27.5° and 27.8°.

In the range 28.5°-29.3° the switching between Modes IIIb and IV is characterized by the alternation between three maxima for the Mode IIIb and a single maximum for the Mode IV. The presence of three maxima holds since $\alpha = 30°$, where their number rises again due to a low frequency modulation. As shown in figure (30), the Lyapunov exponents remain rather small also in the Mode IV regime, thus meaning that up to $\alpha = 40°$, the conditions analyzed are quite stable. At $\alpha = 29.1°$ the Lyapunov exponent related to Mode IV shows a local peak, so that a further stability analysis should be interesting and it is actually

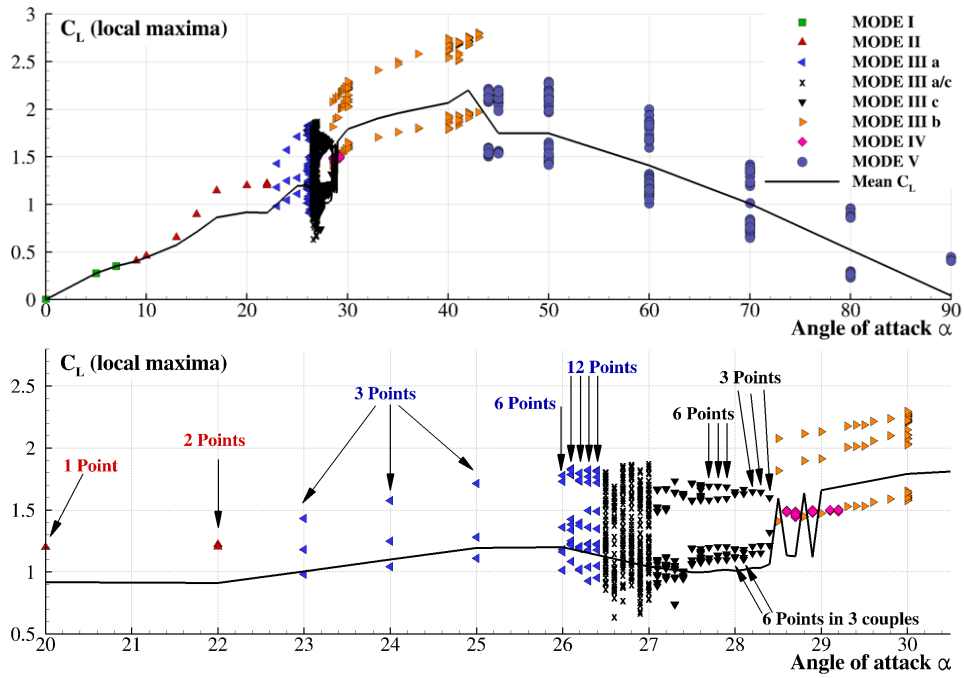

Figure 29: Bifurcation diagram for the α parameter. Top: the whole incidence range. Down: magnification around the AoA where Modes III and IV take place.

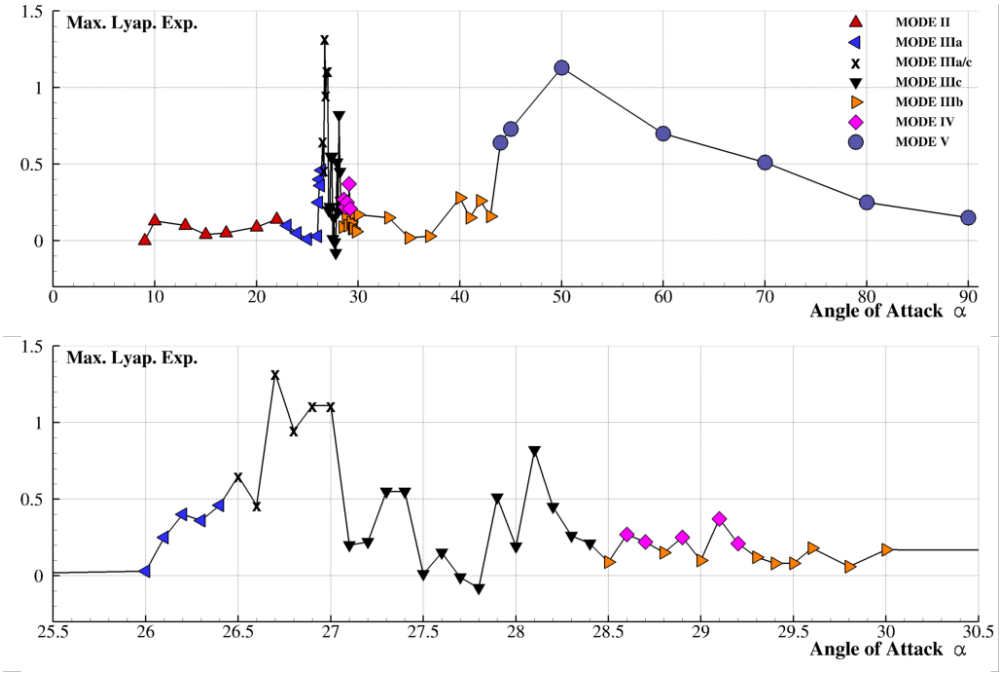

Figure 30: Maximum Lyapunov exponent versus the angle of attack. Top: the whole incidence range. Down: magnification around the AoA where Modes III and IV take place.

dealt with in the next subsection.

For higher AoA, two groups of local lift maxima reappear and the Lyapunov exponents rise up to $\alpha = 50°$. The Mode V reveals to be unstable, as evident also from the phase diagrams in figure (28), although it becomes more and more stable for α increasing, as highlighted by the Lyapunov exponents which decrease with α. The last AoA $\alpha = 90°$, when the lift time signal recasts a monochromatic shape, presents again a single lift maximum.

4.2. Response to a perturbation on the upstream conditions

In the previous section we showed that small variations of the angle of attack, of order 0.1°, can lead to the development of different Modes. Therefore, it can be argued that small perturbations of the flow conditions have a relevant role in the Mode onset. This point is crucial if the same analysis carried out in the present work are investigated with a different approach (both experimental or numerical). To test the stability of the Modes we select the case with $\alpha = 29.1°$ corresponding to a Mode IV condition. Looking at figure (30), the selected α is surrounded by cases belonging to the Mode IIIb and presents also the highest Lyapunov exponent

in this α range. To perturb the Mode IV at $\alpha = 29.1°$ the free-stream direction is changed between $t_1 U/c = 99$ and $t_2 U/c = 101$. Within this interval the angle of attack of the profile passes from 29.1° to 0° at $t = t_1$ and from 0° to 29.1° at $t = t_2$. The effect of this variation is shown in terms of lift force in figure (31) and of wake perturbation in figure (32). The sudden variation of the AoA is evident by the spikes on the top plot of figure (31), which induce an important effect in the wake field (visible in figure (32)). After an initial transient (around $145c/U$), the Mode IV is fully recovered without any appreciable difference respect to the unperturbed condition. This behaviour is highlighted in the bottom plot of figure (31), where the unperturbed signal (shifted forward) is superimposed to the perturbed one. For $tU/c > 150$ the time signals are roughly indistinguishable, thus indicating a significant stability in the Mode IV persistence.

A rigorous conclusion about the stability of the Modes for all the angles of attack considered would require a wider and more deep analysis, changing the perturbation amplitude and duration for each α. On the other hand, the fact that the system comes back to the original regime after a not negligible time lag and in one of the most unstable regimes, leads to believe that the results are even more valid also for other angles of attack.

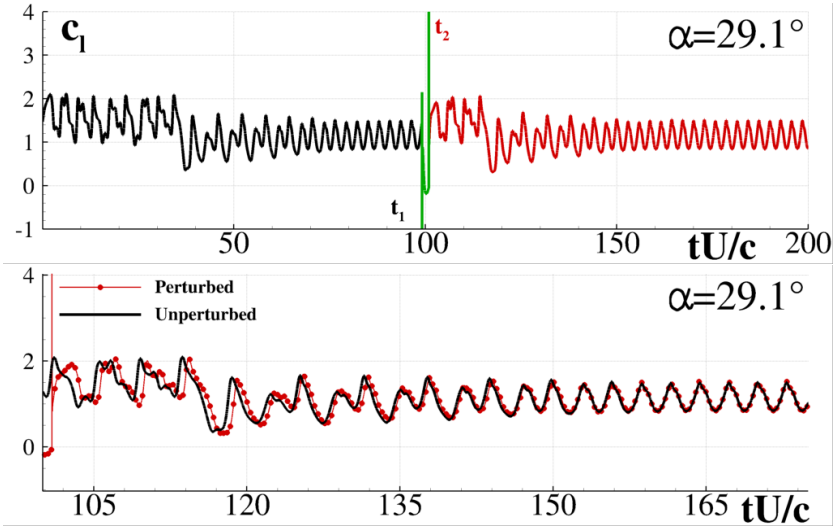

Figure 31: Lift time signal for $\alpha = 29.1°$. Between t_1 and t_2, the angle of attack is varied of $-29.1°$. Top: the lift time signal is drawn in black for $tU/c > t_1$, in green for $t_1 \leq tU/c \leq t_2$ and in red for $tU/c > t_2$. Bottom: comparison between the signal after the perturbation (red solid line with circles) and the same signal before the perturbation (black solid line) shifted of $79.3tU/c$ forward in time.

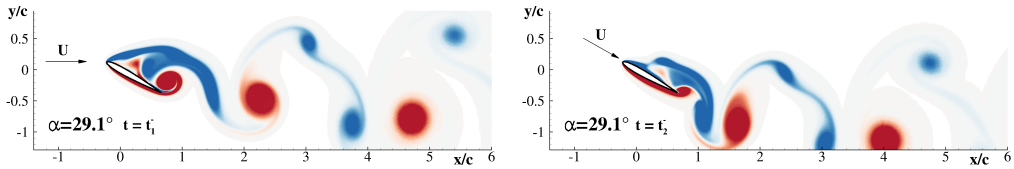

Figure 32: Wake perturbation due to the variation of the free-stream. Top: wake just before perturbation. Bottom: wake just after perturbation. The non-dimensional vorticity contour coloring goes from −5 (blue) to 5 (red).

5. Mean drag and lift coefficients as a function of the angle of attack

As last section the behavior of the mean values of drag and the lift coefficients varying the angle of attack is briefly outlined. Beside the mean values, also the standard deviations of the time signals of the forces have been considered and included in the results. In the figures (33,34,35) the coefficients C_l, C_d and the efficiency L/D are plotted versus to the angles of attack. Different symbols are associated to different Modes in accordance with the previous section, whereas the error bars indicate the standard deviations.

For the Mode I, being the flow attached to the profile, mean values of C_l and C_d show an almost linear behaviour with α and the efficiency grows up to 98% of its maximum value. The latter is reached within the Mode II at $\alpha = 10°$.

For wider angles the efficiency reduces while the lift force starts to oscillate significantly around the mean value. Within Mode II the stall condition takes place. Indeed, for α around 20° the steepness of the lift curve abruptly reduces almost to zero and a plateau of the lift force is observed.

Entering in the Mode IIIa regime, the mean C_l starts to increase again and similarly does the C_d with a wider standard deviation while the efficiency reduces till to ~ 1.62 at $\alpha = 27°$.

For α between 26.5° and 27° the solution changes in time without reaching a stable Mode, alternating chaotically between Mode IIIa and Mode IIIc. Because of this instability, it results in a remarkable standard deviation on both C_l (30%) and C_d (20%).

The Mode IIIc spans just for 1.4° and, within this range, the force coefficients and their standard deviations remain rather constant. Passing from Mode IIIc to Mode IIIb, both the mean values of C_d and C_l suddenly increase through a bifurcation of the solution.

Within the range $\alpha = (28.5° - 29.3°)$ the solution jumps between Mode IIIc and Mode IV under little variations of the angle of attack. The plots in figures 33,34,35

indicate that those Modes belong to two different branches of the solution which pass from one Mode to the other through bifurcation phenomena. The values of drag and lift of the Mode IV are quite close to the ones recorded on the Mode IIIc.

It is worth to stress that, although different Modes are characterized by an evident change of the wake topologies, as shown in previous section 3, a clear bifurcation on the mean forces is well visible only when passing from Mode IIIc to Mode IIIb and from Mode IIIb to Mode IV. Regarding the existing literature, both in Kurtulus (2015) and in Kurtulus (2016) just one bifurcation on the forces was observed when passing from Mode III to Mode IV.

Concluding the current description, the Mode V regime starts at $\alpha = 44°$. The passage from Mode IIIb to Mode V is characterized again by a sudden change on the mean force values, whereas the efficiency L/D does not exhibit any appreciable variation when passing through the Modes. By increasing the angle of attack, the lift force gradually reduces and reaches a null value at $\alpha = 90°$. Conversely, the mean C_d increases up to ~ 3 for $\alpha = 90°$ (this value being in accordance with the work of Najjar and Vanka (1995)). The standard deviation varies around $0.2 - 0.3$

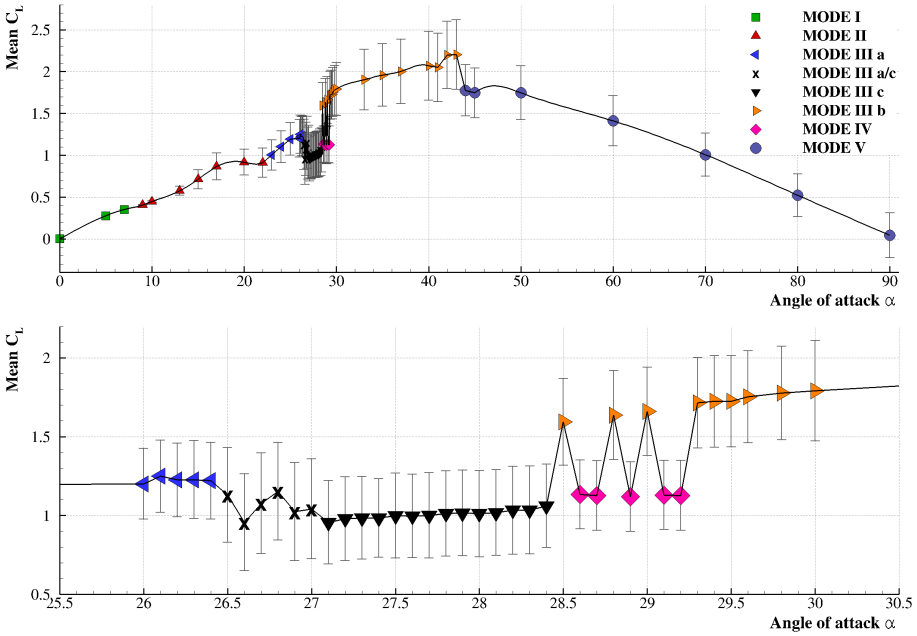

Figure 33: Mean values of Lift coefficient C_l versus the angle of attack. The standard deviations are drawn as error bars. At different Modes are associated different symbols/colours. Top: the whole range of AoA investigated. Bottom: magnification around the Modes III and IV.

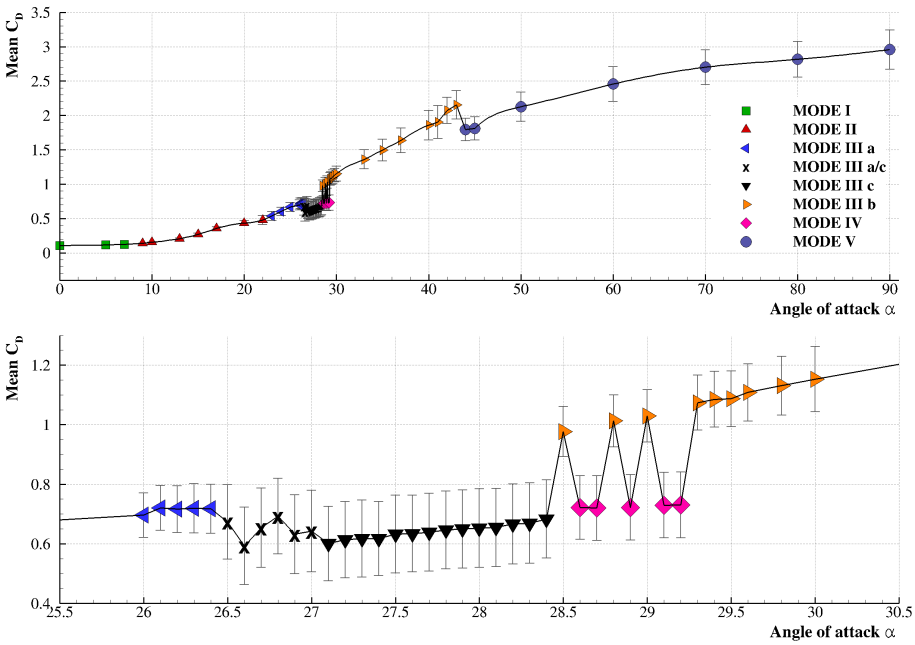

Figure 34: Mean values of the Drag coefficient C_d versus the angle of attack. The standard deviations are drawn as error bars. At different Modes are associated different symbols/colors. Top: the whole range of AoA investigated. Bottom: magnification around the Modes III and IV.

for the mean C_d and $0.25 - 0.30$ for the mean C_l, thus indicating a considerable fluctuation in time of the forces also in this regime.

6. Toward three-dimensional investigations

As stressed in section 1, the 2D approach used in the present paper agrees with former investigations performed by many authors as Pulliam and Vastano (1993); Kurtulus (2015, 2016); Liu et al. (2012) in terms of a dynamical system analysis. The presence of a third dimension introduces an additional parameter related to the spanwise length of the airfoil as well as to the boundary condition in the third dimension (periodic, free slip, fine-dimension airfoil with the presence of the wingtip vortices). The comparisons between 2D and 3D results offered by Lee et al. (2017); Counsil and Goni Boulama (2013); Uranga et al. (2011) assess that the two approaches are in well agreement in terms of the global forces for angles of attack below the stall inception, even for large Reynolds numbers (up to 10^5).

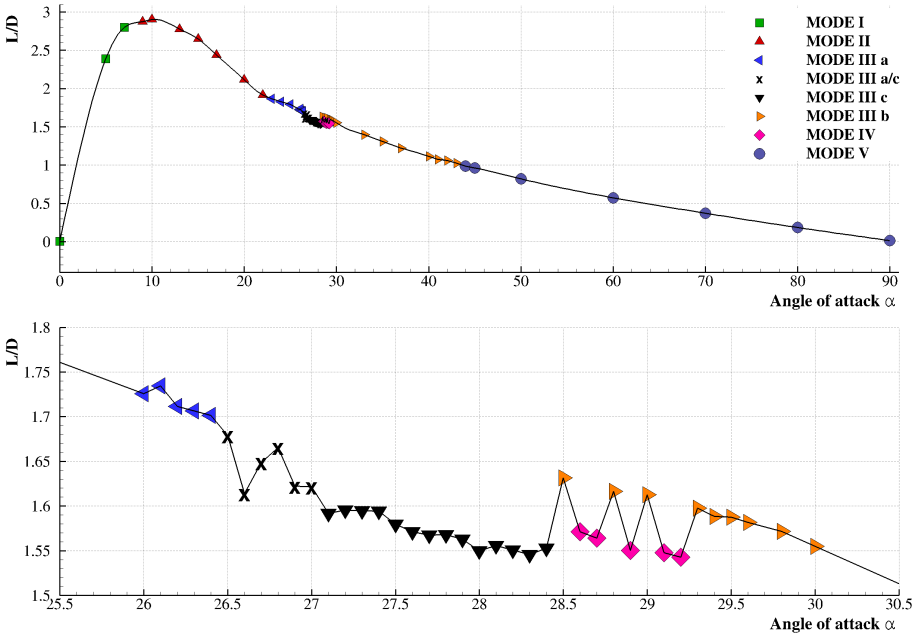

Figure 35: Mean values of efficiency (L/D) versus the angle of attack. At different Modes are associated different symbols/colors. Top: the whole range of AoA investigated. Bottom: magnification around the Modes III and IV.

In the present section we want to stress this concept more by making a comparison between 3D and 2D simulations at $\alpha = 10°$ and $\alpha = 28.5°$. This choice is motivated by the fact that the separation at this Reynolds number is over the 10°, while at 28.5° the regime of the Mode IIIB starts. In section 3.6 it was shown that for this mode the wake is characterized by a strong coherence of the vortex dipoles (see figure 19). Therefore, the existence of this Mode in a 3D context is strictly related to the intensity of the vortex stretching that can disrupt the two-dimensionality of those coherent structures.

In figure 36 the Q-criterion is exploited for highlighting the vortex structures shed by a periodic wing with a spanwise dimension twice the chord length. The case $\alpha = 10°$ shows an evident 2D pattern with vortex tubes unperturbed in the transverse direction. Conversely, the case $\alpha = 28.5°$ is characterized by a significant three-dimensional structure of the flow field with streamwise vortices deforming the shear layers and destabilizing the near field along the spanwise direction.

The time histories of lift signal in both cases are compared in figure 37, where

the agreement between two and three dimensional analysis is evident in for the lower angle case.

The simulations are carried out with a 3D extension of the DVH solver but with a poor resolution with respect to the 2D cases. This is one of the principal drawbacks in performing three-dimensional simulations, becoming prohibitive the total number of vortices in terms of computational resources, as discussed in Appendix B. The possibility to manage high resolution 3D simulations is one of the present on-going activities.

7. Conclusions

In the present work, the flow past a NACA0010 airfoil for varying angle of attack and at Re = 1000 is investigated. The angle of attack α varies from 0° to 90° and the forces time signals are studied in terms of Fourier transforms and phase portrait diagrams of the lift force. The vorticity fields of the different wakes

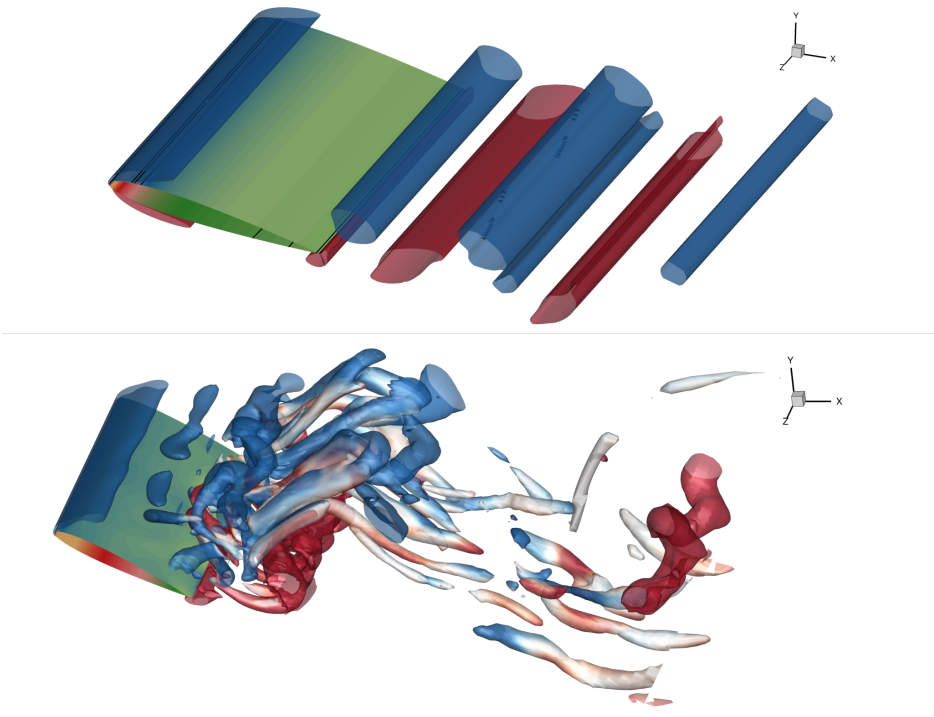

Figure 36: Vortical structures shed by the airfoil obtained with the Q-criterion contoured with transverse vorticity. Top: α = 10.0°. Bottom: α = 28.5°.

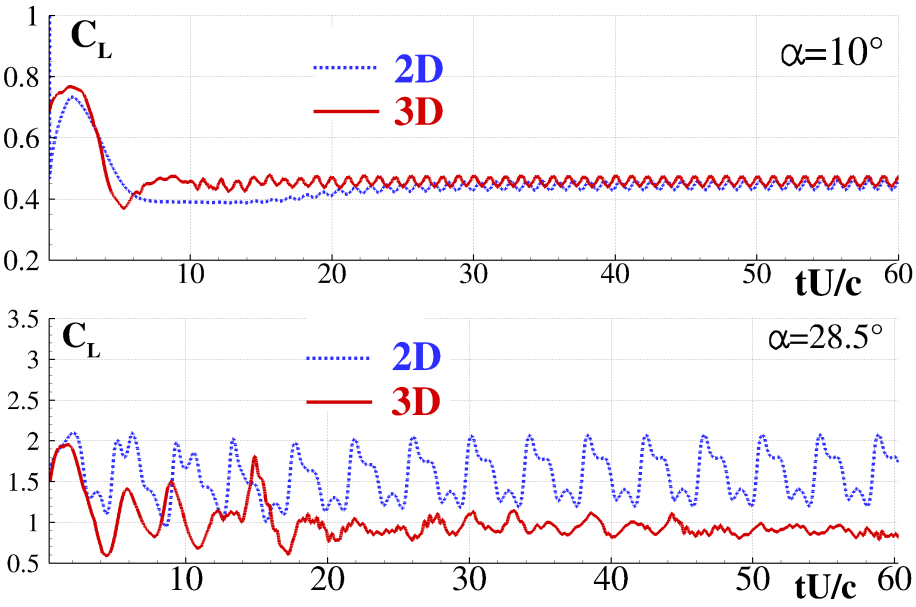

Figure 37: Lift time signals compared between 3D and 2D simulations.

are accurately time resolved by the DVH numerical model. The system is found to undergo different regimes in specific ranges of α, exhibiting simple periodic regimes, doubling/halving period bifurcations, tripling regimes and fully chaotic dynamics.

The gradual increasing of incidence angle has allowed to find a direct cascade to chaos through multiple bifurcations in the forces time histories, where period doubling and tripling phenomena are found in the lift spectra as well as in the C_L local maxima. Differently from the existing literature, in the present work the passages between the different Modes are deeply investigated. From 26.5° to 27° the route to chaos is evident also by the increasing of the Lyapunov exponents and the typical direct enstrophy cascade with the slope of -3 is found. A sudden inverse route from chaos appears by further increasing the AoA up to 28.5°. The presence of a new Mode, called Mode IV, manifesting in a narrow interval only, is found for the first time. In spite of its elusive nature, this Mode has found to be stable to strong perturbations of the angle of attack thus indicating that the system is actually within a new equilibrium state.

In order to show the effect of the third dimension on the present analysis, 3D simulations have been performed for a low AoA $\alpha = 10°$, where a still 2D behavior is found, and for an higher one $\alpha = 28.5°$ where the third dimension

plays a dramatic role in the near wake stability. The prohibitive requirements in terms of computational costs make the parametric analysis performed in the preset work (maintaining the same spatial/temporal resolution) still beyond the present numerical resources.

A further inspection on the role of the profile shape will be the matter of next studies.

Acknowledgments

The research activity has been developed within the Project Area "Applied Mathematics" of the Department of Engineering, ICT and Technology for Energy and Transport (DIITET) of the Italian National Research Council (CNR).

Appendix A. Convergence tests

In the present Section a convergence test is reported in order to highlight the independence of the present solutions by a further increasing of the spatial resolution. In figure A.38, the lift signal calculated at $\alpha = 25°$ is shown for three resolutions $c/\Delta r = 100, 200, 400$ where c is the chord length and Δr the particle size adopted in the near field.

For this test, a stalled angle at which the regime is stable with a clear periodic behavior of the lift force was selected.

Top plot of figure A.38 shows the time histories of the lift coefficient at different resolutions $c/\Delta r$ in the period regime. The signals corresponding to $c/\Delta r = 200$ and 400 give very similar results, while for $c/\Delta r = 100$ a shifting of the solution is found. Table A.1 reports the mean and maximum C_L values varying the resolution: a convergence rate of order about 2 is achieved for the mean values while a rate of about 1 is observed for the maxima. Bottom plot of figure A.38 sketches the Fourier Transform of the same signals, assessing a higher convergence rate for the amplitudes of the first two dominant peaks.

Besides the global forces, also the vorticity fields in the near wakes are compared in figure A.39 where a maximum lift condition is sketched. Consistently with the global forces, the results of the simulations performed at $c/\Delta r = 200$ and 400 are remarkably similar, while for $c/\Delta r = 100$ a wider diffusion of the shear layers is detected.

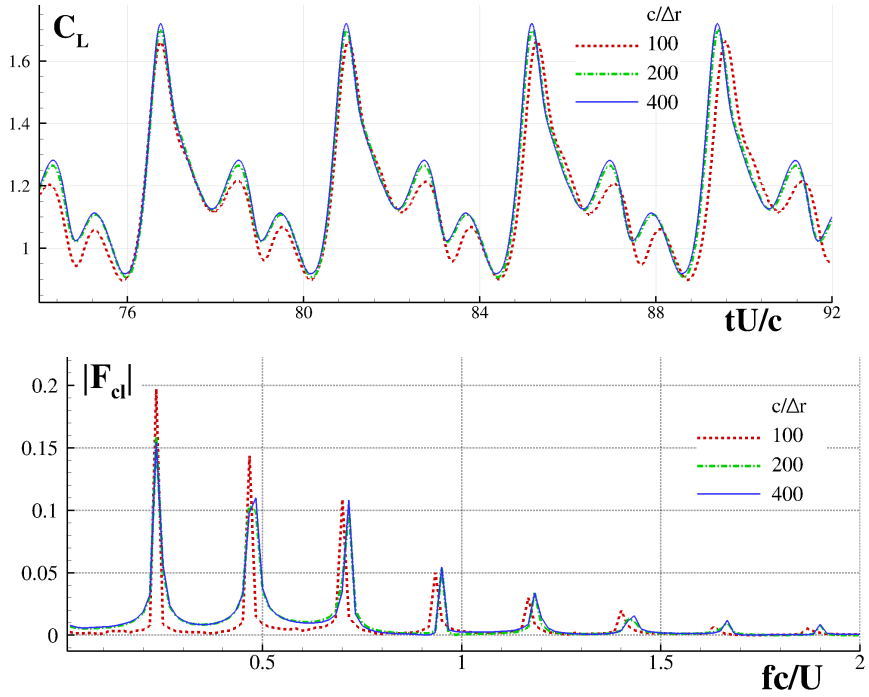

Figure A.38: Convergence tests on lift forces for $\alpha = 25°$ using three different spatial resolution $c/\Delta r = 100, 200, 400$. Top: time histories of the C_L. Bottom: Fourier transform of the C_L.

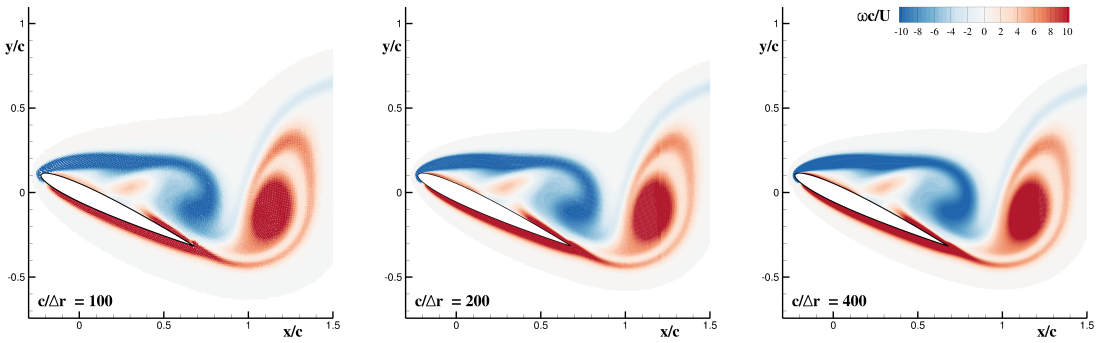

Figure A.39: Convergence tests for $\alpha = 25°$. Vorticity field in the near region using three different spatial resolution $c/\Delta r = 100$ (left), 200 (middle) ,400 (right).

Appendix B. Computational costs

The simulations used in this work have been all performed on 8 cluster nodes (2*18-core Intel Xeon E5-2697 v4 2.30GHz), through an OpenMP parallel

$c/\Delta r$	$\overline{C}_L$	Differences	$C_{L\,Max}$	Differences
100	1.162	–	1.660	–
200	1.188	0.026	1.698	0.038
400	1.194	0.006	1.720	0.022

Table A.1: Convergence of the mean and maximum values of the lift coefficient.

interface programming. The CPU costs of the implemented algorithm for 2D cases are about 100μs per vortex particle and per time iteration on a single core. These costs rise up to about 600μs in 3D.

It is worth to stress that, although the analysis carried out in the present work is mainly confined to a two-dimensional framework, the fine spatial resolutions adopted, as well as the long-time evolution, determined a demanding computational costs.

Indeed, to perform 70 simulations with 2 million vortices for 80,000 time iterations, the net computational cost amounts to about two months. This cost is inline with other vortex particle solvers and it is grossly affected by the Fast Multipole Method for the solution of the Poisson equation, being the largest number of used particles of order 10^6 and the allocated memory not exceeding 1 Gbyte.

The computational costs in 3D framework would require up to 1.6 billion of particles, if the same spatial resolution of the 2D simulation is adopted. At the present stage, the DVH algorithm is not able to manage this huge number of particles, hence, as highlighted in Section 6, the spatial resolution has been scaled by a factor 4 (*i.e.* $c/\Delta r = 100$) in every direction, thus reducing the total number of vortices to 25 million in the near-field. The CPU costs of a single simulation are so limited to 45 days on a single cluster node. Concluding, three-dimensional investigations varying the parameter α remain still prohibitive to the present numerical resources.

References

Alam, M. M., Zhou, Y., Yang, H., Guo, H., Mi, J., 2010. The ultra-low Reynolds number airfoil wake. Experiments in fluids 48 (1), 81–103.

Badrinath, S., Bose, C., Sarkar, S., 2017. Identifying the route to chaos in the flow past a flapping airfoil. European Journal of Mechanics-B/Fluids 66, 38–59.

Bao, Y., Zhou, D., Tao, J., Peng, Z., Zhu, H., Sun, Z., Tong, H., 2017. Dynamic interference of two anti-phase flapping foils in side-by-side arrangement in an incompressible flow. Physics of Fluids 29 (3), 033601.

Barba, L. A., Leonard, A., Allen, C. B., 2003. Numerical investigations on the accuracy of the vortex method with and without remeshing. AIAA paper 3426.

Benson, M., Bellamy-Knights, P., Gerrard, J., Gladwell, I., 1989. A viscous splitting algorithm applied to low Reynolds number flows round a circular cylinder. Journal of Fluids and Structures 3 (5), 439–479.

Boffetta, G., Ecke, R. E., 2012. Two-dimensional turbulence. Annual Review of Fluid Mechanics 44, 427–451.

Bose, C., Sarkar, S., 2018. Investigating chaotic wake dynamics past a flapping airfoil and the role of vortex interactions behind the chaotic transition. Physics of Fluids 30 (4), 047101.

Chorin, A., 1973. Numerical study of slightly viscous flow. Journal of Fluid Mechanics 57 (04), 785–796.

Chorin, A., 1978. Vortex sheet approximation of boundary layers. Journal of Computational Physics 27 (3), 428–442.

Colagrossi, A., Bouscasse, B., Antuono, M., Marrone, S., 2012. Particle packing algorithm for SPH schemes. Computer Physics Communications 183 (2), 1641–1683.

Colagrossi, A., Rossi, E., Marrone, S., Le Touzé, D., 2016. Particle Methods for Viscous Flows: Analogies and Differences Between the SPH and DVH Methods. Communications in Computational Physics 20 (3), 660–688.

Counsil, J. N., Goni Boulama, K., 2013. Low-reynolds-number aerodynamic performances of the naca 0012 and selig–donovan 7003 airfoils. Journal of aircraft 50 (1), 204–216.

Cruz, F. A., Barba, L., 2009. Characterization of the accuracy of the fast multipole method in particle simulations. International journal for numerical methods in engineering 79 (13), 1577–1604.

Das, A., Shukla, R. K., Govardhan, R. N., 2016. Existence of a sharp transition in the peak propulsive efficiency of a low-Re pitching foil. Journal of Fluid Mechanics 800, 307–326.

Deng, J., Sun, L., Shao, X., 2019. Wake dynamics of low-reynolds-number flow around a two-dimensional airfoil. Physics of Fluids 31 (2), 024102.

Durante, D., Rossi, E., Colagrossi, A., Graziani, G., 2016. Numerical simulations of the transition from laminar to chaotic behaviour of the planar vortex flow past a circular cylinder. Communications in Nonlinear Science and Numerical Simulation 48, 18–38.

Fayed, M., Portaro, R., Gunter, A.-L., Abderrahmane, H. A., Ng, H. D., 2011. Visualization of flow patterns past various objects in two-dimensional flow using soap film. Physics of Fluids 23 (9), 091104.

Jia, L., Xiao, Q., Wu, H., Wu, Y., Yin, X., 2015. Response of a flexible filament in a flowing soap film subject to a forced vibration. Physics of Fluids 27 (1), 017101.

Jones, K., Dohring, C., Platzer, M., 1998. Experimental and computational investigation of the knoller-betz effect. AIAA journal 36 (7), 1240–1246.

Khalid, M. S. U., Akhtar, I., 2012. Characteristics of flow past a symmetric airfoil at low Reynolds number: a nonlinear perspective. In: Proceedings of the ASME 2012 international mechanical engineering congress & exposition IMECE. Vol. 87389. pp. 9–15.

Krishnan, H., Agrawal, A., Sharma, A., Sheridan, J., 2016. Near-body vorticity dynamics of a square cylinder subjected to an inline pulsatile free stream flow. Physics of Fluids 28 (9), 093605.

Kurtulus, D. F., 2015. On the Unsteady Behavior of the Flow Around NACA 0012 Airfoil with Steady External Conditions at Re= 1000. International Journal of Micro Air Vehicles 7 (3), 301–326.

Kurtulus, D. F., 2016. On the wake pattern of symmetric airfoils for different incidence angles at Re= 1000. International Journal of Micro Air Vehicles 8 (2), 109–139.

Lee, D., Nonomura, T., Oyama, A., Fujii, K., 2017. Comparative studies of numerical methods for evaluating aerodynamic characteristics of two-dimensional airfoil at low reynolds numbers. International Journal of Computational Fluid Dynamics 31 (1), 57–67.

Leonov, G. A., Kuznetsov, N. V., 2007. Time-varying linearization and the perron effects. International journal of bifurcation and chaos 17 (04), 1079–1107.

Liu, Y., Li, K., Zhang, J., Wang, H., Liu, L., 2012. Numerical bifurcation analysis of static stall of airfoil and dynamic stall under unsteady perturbation. Communications in Nonlinear Science and Numerical Simulation 17 (8), 3427–3434.

Mandujano, F., Málaga, C., 2018. On the forced flow around a rigid flapping foil. Physics of Fluids 30 (6), 061901.

Melander, M., McWilliams, J., Zabusky, N., 1987. Axisymmetrization and vorticity-gradient intensification of an isolated two-dimensional vortex through filamentation. Journal of Fluid Mechanics 178, 137–159.

Najjar, F. M., Vanka, S., 1995. Simulations of the unsteady separated flow past a normal flat plate. International Journal for Numerical Methods in Fluids 21 (7), 525–547.

Nayfeh, A. H., Balachandran, B., 2008. Applied nonlinear dynamics: analytical, computational, and experimental methods. John Wiley & Sons.

Pulliam, T. H., Vastano, J. A., 1993. Transition to chaos in an open unforced 2D flow. Journal of Computational Physics 105 (1), 133–149.

Riccardi, G., Durante, D., 2006. Elementi di fluidodinamica. Springer-Verlag Italia.

Rossi, E., Colagrossi, A., Bouscasse, B., Graziani, G., 2015a. The Diffused Vortex Hydrodynamics method. Communications in Computational Physics 18 (2), 351–379.

Rossi, E., Colagrossi, A., Durante, D., Graziani, G., 2016. Simulating 2d viscous flow around geometries with vertices through the diffused vortex hydrodynamics method. Computer Methods in Applied Mechanics and Engineering 302, 147–169.

Rossi, E., Colagrossi, A., Graziani, G., 2015b. Numerical Simulation of 2D-Vorticity Dynamics using Particle Methods. Computers and Mathematics with Applications 69 (12), 1484–1503.

Rossi, E., Colagrossi, A., Oger, G., LeTouzé, D., 2018. Multiple bifurcations of the flow over stalled airfoils changing the Reynold numbers. Journal of Fluid Mechanics 846, 356–391.

Saffman, P. G., 1992. Vortex dynamics. Cambridge university press.

Schnipper, T., Andersen, A., Bohr, T., 2009. Vortex wakes of a flapping foil. Journal of Fluid Mechanics 633, 411–423.

Tian, X., Ong, M. C., Yang, J., Myrhaug, D., 2011. Two-dimensional numerical simulation of flow around rectangular structures with different aspect ratios. In: ASME 2011 30th International Conference on Ocean, Offshore and Arctic Engineering. American Society of Mechanical Engineers, pp. 395–403.

Uranga, A., Persson, P.-O., Drela, M., Peraire, J., 2011. Implicit large eddy simulation of transition to turbulence at low reynolds numbers using a discontinuous galerkin method. International Journal for Numerical Methods in Engineering 87 (1-5), 232–261.

Wang, K., Yang, L., Yu, Y., Hou, G., 2018. Influence of slip boundary on the hydrofoil with a curved slip boundary condition for the lattice boltzmann method. Physics of Fluids 30 (12), 123601.

Williamson, C., Govardhan, R., 2004. Vortex-induced vibrations. Annu. Rev. Fluid Mech. 36, 413–455.

Wolf, A., Swift, J. B., Swinney, H. L., Vastano, J. A., 1985. Determining lyapunov exponents from a time series. Physica D: Nonlinear Phenomena 16 (3), 285–317.

Ye, H., Wei, H., Huang, H., Lu, X.-y., 2017. Two tandem flexible loops in a viscous flow. Physics of Fluids 29 (2), 021902.